

## Localization of nuclear wave functions of lithium in $[\text{Li}^+\text{@C}_{60}]\text{PF}_6^-$ : molecular insights into two-site disorder–order transition

Hideo Ando<sup>1, a)</sup> and Yoshihide Nakao<sup>2</sup>

<sup>1)</sup> Faculty of Science, Yamagata University, 1-4-12 Kojirakawa-machi, Yamagata, Yamagata 990-8560, Japan.

<sup>2)</sup> Faculty of Life Science, Kyushu Sangyo University, 2-3-1 Matsukadai, Higashi-ku, Fukuoka 813-8503, Japan.

(Dated: 27 February 2023)

---

Tables S1, S2	...	Positions of the ring centers
Tables S3, S4	...	The parameters and RMSEs of the potential energy function
Tables S5, S6	...	Positions of the C atoms
Table S7	...	Potential energy minima and related quantities
Tables S8, S9	...	Potential and interaction energies of $\text{Li}^+$ placed underneath every ring center
Fig. S1	...	Crystal structure of $[\text{Li}^+\text{@C}_{60}]\text{PF}_6^-$ at 6 K
Fig. S2	...	Unwrapped geometry of the $\text{C}_{60}$ cage and the symbols for the cage-surface points
Fig. S3	...	Radial distance $r_{\text{C}}$ of every C atom
Fig. S4	...	Radial displacement $\Delta r_{\text{C}}$ of every C atom in the 6 K geometry relative to that in the 40 K geometry
Fig. S5–S9	...	Radial, polar, and isosurface plots of the potential energy function (see p. 17 for the detailed analysis of Fig. S8)
Fig. S10	...	Fragment pair decomposition of Fig. 4
Fig. S11, S12	...	Overlap matrix and norms for the nuclear wave functions of $\text{Li}^+$
Fig. S13	...	Nuclear energy levels of $\text{Li}^+$
Fig. S14, S15	...	Low-energy nuclear wave functions of $\text{Li}^+$
Fig. S16, S17	...	Accuracy of the approximation of the dipole moment, $\boldsymbol{\mu} \propto \boldsymbol{x}$ (see p. 28 for the detailed explanation of the results)
Fig. S18, S19	...	Stick absorption spectra in the THz frequency range and the spectral contributions of the transitions from the ground state

---

<sup>a)</sup> Author to whom correspondence should be addressed. Electronic mail: ando@sci.kj.yamagata-u.ac.jp

Table S1. Positions of the ring centers in the northern hemisphere ( $z > 0$ ) of the  $[\text{Li}^+\text{@C}_{60}]\text{6PF}_6^-$  (6 K) model. The distance and the inclination angle from the polar  $z$  axis ( $d_{\text{ring-z}}$  and  $\theta_{\text{ring}}$ , respectively) are listed. See Fig. S2 for the map of the individual ring-center points.

	$d_{\text{ring-z}}$ (Å)	$\theta_{\text{ring}}$ (deg.)
C <sub>6</sub> (1)	0.0000	0.00
C <sub>6</sub> (2)	2.1597	41.76
C <sub>6</sub> (3)	3.0548	70.53
C <sub>6</sub> (4)	3.0556	70.55
C <sub>5</sub> (1)	2.0167	37.36
C <sub>5</sub> (2)	3.2552	79.23

Table S2. Positions of the ring centers in the southern hemisphere ( $z < 0$ ) of the  $[\text{Li}^+\text{@C}_{60}]\text{6PF}_6^-$  (6 K) model. The distance and the inclination angle from the polar  $z$  axis ( $d_{\text{ring-z}}$  and  $\theta_{\text{ring}}$ , respectively) are listed. See Fig. S2 for the map of the individual ring-center points.

	$d_{\text{ring-z}}$ (Å)	$\theta_{\text{ring}}$ (deg.)
C <sub>6</sub> (1')	0.0000	180.00
C <sub>6</sub> (2')	2.1596	138.22
C <sub>6</sub> (3')	3.0564	109.48
C <sub>6</sub> (4')	3.0562	109.50
C <sub>5</sub> (1')	2.0162	142.60
C <sub>5</sub> (2')	3.2558	100.84

Table S3. Modified Morse parameters in  $V_{\text{es+exrep+pol+disp}}^{6\text{K}}$ , optimized for the RI-MP2 potential energy surface ( $\Delta E_{\text{RI-MP2}}$ ) of the  $[\text{Li}^+@\text{C}_{60}]\text{6PF}_6^-$  (6 K) model.

	$D_e^j$ (kcal mol $^{-1}$ )	$\alpha_e^j$ ( $\text{\AA}^{-1}$ )	$s_e^j$ ( $\text{\AA}$ )
Northern hemisphere ( $z > 0$ )			
C $^1$ ( $j = 1$ ) <sup>a</sup>	11.764702790	1.339520160	2.131371817
C $^2$ ( $j = 2$ )	12.065560387	1.340281448	2.127456790
C $^3$ ( $j = 3$ )	11.655134449	1.345121171	2.141503214
C $^4$ ( $j = 4$ )	13.190316562	1.345120896	2.114532724
C $^5$ ( $j = 5$ )	13.675591433	1.295705150	2.131449029
C $^6$ ( $j = 6$ )	13.304922653	1.335185291	2.114920270
C $^7$ ( $j = 7$ )	13.371300359	1.292411352	2.134824197
C $^8$ ( $j = 8$ )	10.428838376	1.395059889	2.148789360
C $^9$ ( $j = 9$ )	11.033897067	1.461715225	2.121967921
C $^{10}$ ( $j = 10$ )	10.556788068	1.397809697	2.144502353
Southern hemisphere ( $z < 0$ )			
C $^{1'}$ ( $j = 1'$ ) <sup>a</sup>	11.297298762	1.345349879	2.141738419
C $^{2'}$ ( $j = 2'$ )	12.157293083	1.354097930	2.124597269
C $^{3'}$ ( $j = 3'$ )	10.820224272	1.315326942	2.157708310
C $^{4'}$ ( $j = 4'$ )	13.264930492	1.348134503	2.113465207
C $^{5'}$ ( $j = 5'$ )	13.621260482	1.285723294	2.132312887
C $^{6'}$ ( $j = 6'$ )	13.879997633	1.358183332	2.104213286
C $^{7'}$ ( $j = 7'$ )	12.713013572	1.296648454	2.143108817
C $^{8'}$ ( $j = 8'$ )	11.158689573	1.399284460	2.135458185
C $^{9'}$ ( $j = 9'$ )	11.988715990	1.466621523	2.106141490
C $^{10'}$ ( $j = 10'$ )	11.492574842	1.411550527	2.129725717
	$V_{\text{shift}}$ (kcal mol $^{-1}$ )	$\zeta$	
	5.811323972	-0.619699276	

<sup>a</sup> See Fig. S2 for the positions of the C $^j$  atoms ( $j = 1, \dots, 10, 1', \dots, 10'$ ).

Table S4. The root-mean-square errors (RMSEs) of the potential energy function  $V_{\text{es+exrep+pol+disp}}^{6\text{K}}$  for the  $[\text{Li}^+\text{@C}_{60}]\text{6PF}_6^-$  (6 K) model and the  $V_{\text{es+exrep+pol+disp}}^{6\text{K}}$  energy at the  $\text{C}_{60}$  cage center. All values are given in  $\text{kcal mol}^{-1}$ . The optimized model parameters are listed in Table S3.

	$V_{\text{es+exrep+pol+disp}}^{6\text{K}}$
Energy at the cage center	-0.77160
RMSE ( $-7.0 \text{ kcal mol}^{-1}$ )	0.05658
RMSE ( $-5.0 \text{ kcal mol}^{-1}$ ) <sup>a</sup>	0.12291
RMSE ( $-3.0 \text{ kcal mol}^{-1}$ ) <sup>a</sup>	0.25112
RMSE ( $0.0 \text{ kcal mol}^{-1}$ ) <sup>a</sup>	0.51060

<sup>a</sup> Only the  $\Delta E_{\text{RI-MP2}}$  grid data below an energy threshold of  $-7.0 \text{ kcal mol}^{-1}$  were considered in the Levenberg–Marquardt fitting procedure. The RMSEs shown here are the values calculated using more  $\Delta E_{\text{RI-MP2}}$  grid data, without modifying the potential energy function obtained. For example, RMSE ( $0.0 \text{ kcal mol}^{-1}$ ) was calculated using all of the  $\Delta E_{\text{RI-MP2}}$  grid data below  $0.0 \text{ kcal mol}^{-1}$ , including the data at the cage center. Such an RMSE can be thought of as a measure of the reliability of the potential energy function in a higher energy region.

Table S5. Positions of the C atoms in the northern hemisphere ( $z > 0$ ) of the  $[\text{Li}^+\text{@C}_{60}]\text{6PF}_6^-$  (6 K) model. The distance from the cage center ( $r_C$ ) and the inclination angle from the polar  $z$  axis ( $\theta_C$ ) are listed. We arranged the data in such a way that the  $r_C$  distances are sorted in descending order. See Fig. S2 for the map of the individual C atoms and Fig. S3b for the bubble chart of  $r_C$ .

	$r_C$ (Å)	$\theta_C$ (deg.)
C <sup>1</sup>	3.5498	23.67
C <sup>2</sup>	3.5490	23.60
C <sup>4</sup>	3.5437	47.19
C <sup>6</sup>	3.5417	47.21
C <sup>3</sup>	3.5415	57.75
C <sup>9</sup>	3.5408	80.44
C <sup>10</sup>	3.5361	86.02
C <sup>8</sup>	3.5342	85.99
C <sup>7</sup>	3.5305	63.12
C <sup>5</sup>	3.5284	63.08

Table S6. Positions of the C atoms in the southern hemisphere ( $z < 0$ ) of the  $[\text{Li}^+\text{@C}_{60}]\text{6PF}_6^-$  (6 K) model. The distance from the cage center ( $r_C$ ) and the inclination angle from the polar  $z$  axis ( $\theta_C$ ) are listed. We arranged the data in such a way that the  $r_C$  distances are sorted in descending order. See Fig. S2 for the map of the individual C atoms and Fig. S3b for the bubble chart of  $r_C$ .

	$r_C$ (Å)	$\theta_C$ (deg.)
C <sup>9'</sup>	3.5446	99.59
C <sup>3'</sup>	3.5429	122.20
C <sup>2'</sup>	3.5425	156.30
C <sup>1'</sup>	3.5425	156.35
C <sup>6'</sup>	3.5416	132.80
C <sup>10'</sup>	3.5385	94.08
C <sup>4'</sup>	3.5379	132.78
C <sup>8'</sup>	3.5379	94.04
C <sup>7'</sup>	3.5341	116.98
C <sup>5'</sup>	3.5323	116.94

Table S7. Potential energy minima with respect to  $r$  along the radial rays. For the ring’s center rays, C atom rays, C=C center rays, and C–C center rays, the mean depth and the mean radial distance of the minima,  $\bar{E}_{\min}$  and  $\bar{r}_{\min}$ , are given in kcal mol<sup>-1</sup> and Å, respectively. We also listed the standard deviation of the depths,  $\sigma(E_{\min})$ , that of the radial distances,  $\sigma(r_{\min})$ , and the relevant figure numbers for the reader’s reference. Without parentheses are the values for the  $\Delta E_{\text{RI-MP2}}$  grid data, whereas in parentheses are those for the model function  $V_{\text{es+exrep+pol+disp}}^{6\text{K}}$ . To locate the energy minimum of a ray, we evenly spaced evaluation points on the ray; the distance between any neighboring points is 0.0625 and 0.0125 Å for  $\Delta E_{\text{RI-MP2}}$  and  $V_{\text{es+exrep+pol+disp}}^{6\text{K}}$ , respectively.

	$\bar{E}_{\min}$	$\sigma(E_{\min})$	$\bar{r}_{\min}$	$\sigma(r_{\min})$	Figure
Northern hemisphere ( $z > 0$ )					
ring centers	-10.36 (-10.33)	0.206 (0.218)	1.379 (1.391)	0.015 (0.015)	Fig. S5a
C atoms	-10.08 (-10.12)	0.197 (0.186)	1.363 (1.365)	0.025 (0.009)	Fig. S5b
C=C centers <sup>a</sup>	-10.09 (-10.16)	0.178 (0.169)	1.375 (1.370)	0.000 (0.010)	Fig. S5c
C–C centers	-10.12 (-10.13)	0.204 (0.193)	1.375 (1.368)	0.000 (0.011)	Fig. S5d
Southern hemisphere ( $z < 0$ )					
ring centers	-10.18 (-10.15)	0.117 (0.143)	1.375 (1.389)	0.000 (0.016)	Fig. S6a
C atoms	-9.91 (-9.95)	0.099 (0.091)	1.369 (1.365)	0.019 (0.009)	Fig. S6b
C=C centers	-9.93 (-10.00)	0.099 (0.090)	1.375 (1.368)	0.000 (0.006)	Fig. S6c
C–C centers	-9.95 (-9.96)	0.094 (0.087)	1.375 (1.365)	0.000 (0.008)	Fig. S6d

<sup>a</sup> Although the C<sup>8'</sup>=C<sup>10</sup> ray was considered here, the  $S_6 \rightarrow C_3$  cage distortion makes the corresponding bond center move from the northern to the southern hemisphere across the equator.

Table S8. Potential energies and interaction energies (kcal mol<sup>-1</sup>) of the [Li<sup>+</sup>@C<sub>60</sub>]6PF<sub>6</sub><sup>-</sup> (6 K) model, with Li<sup>+</sup> placed right underneath the individual ring centers in the northern hemisphere ( $z > 0$ ). Every interaction energy is further decomposed into fragment pair interaction energies and a many-body one.<sup>a</sup> All energies are relative to the reference energies at  $r = 0$  Å (*i.e.*, the energies of the geometry with Li<sup>+</sup> at the C<sub>60</sub> cage center). The mean distance between Li<sup>+</sup> and the nearby ring’s C atoms ( $d_{\text{Li-C}}$ ) is also given in Å. Values without parentheses and those in parentheses were calculated for the geometries in which Li<sup>+</sup> is located at  $r = 1.375$  and 1.4375 Å, respectively.

	C <sub>6</sub> (1)	C <sub>6</sub> (2)	C <sub>6</sub> (3)	C <sub>6</sub> (4)	C <sub>5</sub> (1)	C <sub>5</sub> (2)
$d_{\text{Li-C}}$	2.355 ( 2.306)	2.347	2.345	2.345	2.306	2.296
$V_{\text{es+exrep+pol+disp}}^{6\text{K}}$	-10.68 (-10.72)	-10.46	-10.38	-10.32	-10.35	-9.91
$\Delta E_{\text{RI-MP2}}$	-10.72 (-10.73)	-10.51	-10.40	-10.34	-10.43	-9.97
$\Delta E_{\text{es}}^{\text{b}}$	-0.87 ( -0.90)	-0.89	-0.45	-0.39	-0.09	0.32
Li <sup>+</sup> ... C <sub>60</sub>	-0.73 ( -0.76)	-0.59	-0.51	-0.44	0.02	0.34
Li <sup>+</sup> ... 6PF <sub>6</sub> <sup>-</sup>	-0.15 ( -0.14)	-0.30	0.06	0.04	-0.11	-0.03
$\Delta E_{\text{exrep}}$	11.50 ( 13.92)	11.80	11.86	11.83	11.93	12.24
Li <sup>+</sup> ... C <sub>60</sub>	11.44 ( 13.85)	11.78	11.88	11.84	11.91	12.25
Li <sup>+</sup> ... 6PF <sub>6</sub> <sup>-</sup>	0.00 ( 0.00)	0.00	0.00	0.00	0.00	0.00
Many-body effects	0.06 ( 0.07)	0.03	-0.02	-0.01	0.02	-0.01
$\Delta E_{\text{pol}}$	-20.76 (-23.12)	-20.78	-21.01	-20.98	-21.30	-21.39
Li <sup>+</sup> ... C <sub>60</sub>	-20.67 (-23.00)	-20.94	-21.05	-21.04	-21.26	-21.56
Li <sup>+</sup> ... 6PF <sub>6</sub> <sup>-</sup>	-0.32 ( -0.35)	-0.35	-0.25	-0.25	-0.30	-0.27
Many-body effects	0.22 ( 0.23)	0.50	0.30	0.32	0.26	0.45
$\Delta E_{\text{disp}}$	-0.59 ( -0.63)	-0.64	-0.81	-0.80	-0.97	-1.14
Li <sup>+</sup> ... C <sub>60</sub>	-0.83 ( -0.90)	-0.84	-0.85	-0.85	-1.14	-1.19
Li <sup>+</sup> ... 6PF <sub>6</sub> <sup>-</sup>	-0.12 ( -0.13)	-0.15	-0.13	-0.14	-0.13	-0.14
Many-body effects	0.36 ( 0.39)	0.36	0.17	0.19	0.30	0.20

<sup>a</sup> Although there is a fragment pair of C<sub>60</sub> ... 6PF<sub>6</sub><sup>-</sup>, its contribution is zero due to the assumption of frozen intrafragment geometries and therefore omitted in the table.

<sup>b</sup> Because the electrostatic energy is pairwise additive in the EDA scheme, there are no many-body effects for  $\Delta E_{\text{es}}$ .

Table S9. Potential energies and interaction energies (kcal mol<sup>-1</sup>) of the [Li<sup>+</sup>@C<sub>60</sub>]6PF<sub>6</sub><sup>-</sup> (6 K) model, with Li<sup>+</sup> placed right underneath the individual ring centers in the southern hemisphere ( $z < 0$ ). Every interaction energy is further decomposed into fragment pair interaction energies and a many-body one.<sup>a</sup> All energies are relative to the reference energies at  $r = 0$  Å (*i.e.*, the energies of the geometry with Li<sup>+</sup> at the C<sub>60</sub> cage center). The mean distance between Li<sup>+</sup> and the nearby ring’s C atoms ( $d_{\text{Li-C}}$ ) is also given in Å. In any of the geometries, Li<sup>+</sup> is located at  $r = 1.375$  Å.

	C <sub>6</sub> (1')	C <sub>6</sub> (2')	C <sub>6</sub> (3')	C <sub>6</sub> (4')	C <sub>5</sub> (1')	C <sub>5</sub> (2')
$d_{\text{Li-C}}$	2.349	2.345	2.345	2.346	2.303	2.298
$V_{\text{es+exrep+pol+disp}}^{6\text{K}}$	-10.33	-10.22	-10.19	-10.25	-10.04	-9.91
$\Delta E_{\text{RI-MP2}}$	-10.36	-10.26	-10.21	-10.27	-10.12	-9.97
$\Delta E_{\text{es}}^{\text{b}}$	-0.35	-0.44	-0.11	-0.20	0.42	0.36
Li <sup>+</sup> ... C <sub>60</sub>	-0.48	-0.36	-0.27	-0.33	0.32	0.32
Li <sup>+</sup> ... 6PF <sub>6</sub> <sup>-</sup>	0.13	-0.08	0.16	0.12	0.10	0.04
$\Delta E_{\text{exrep}}$	11.79	11.88	11.80	11.80	12.07	12.19
Li <sup>+</sup> ... C <sub>60</sub>	11.70	11.83	11.81	11.80	12.02	12.20
Li <sup>+</sup> ... 6PF <sub>6</sub> <sup>-</sup>	0.00	0.00	0.00	0.00	0.00	0.00
Many-body effects	0.09	0.05	0.00	0.00	0.05	-0.01
$\Delta E_{\text{pol}}$	-21.18	-21.01	-21.06	-21.03	-21.56	-21.39
Li <sup>+</sup> ... C <sub>60</sub>	-20.89	-21.01	-21.04	-21.03	-21.37	-21.52
Li <sup>+</sup> ... 6PF <sub>6</sub> <sup>-</sup>	-0.29	-0.32	-0.24	-0.24	-0.28	-0.26
Many-body effects	0.01	0.33	0.22	0.25	0.08	0.39
$\Delta E_{\text{disp}}$	-0.63	-0.69	-0.85	-0.84	-1.04	-1.14
Li <sup>+</sup> ... C <sub>60</sub>	-0.86	-0.88	-0.88	-0.89	-1.20	-1.19
Li <sup>+</sup> ... 6PF <sub>6</sub> <sup>-</sup>	-0.11	-0.14	-0.13	-0.13	-0.12	-0.14
Many-body effects	0.34	0.34	0.17	0.18	0.29	0.19

<sup>a</sup> Although there is a fragment pair of C<sub>60</sub> ... 6PF<sub>6</sub><sup>-</sup>, its contribution is zero due to the assumption of frozen intrafragment geometries and therefore omitted in the table.

<sup>b</sup> Because the electrostatic energy is pairwise additive in the EDA scheme, there are no many-body effects for  $\Delta E_{\text{es}}$ .

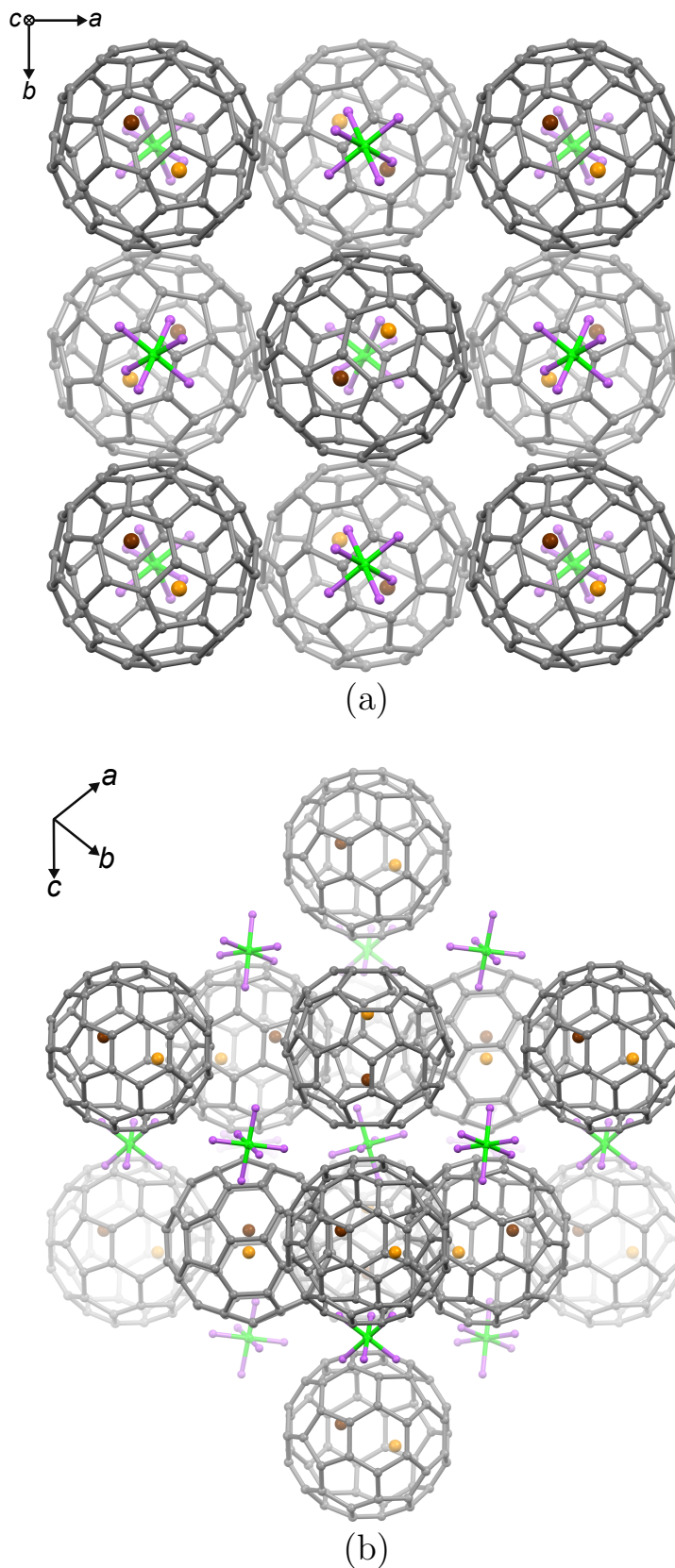


Fig. S1. Crystal structure of  $[\text{Li}^+\text{@C}_{60}]\text{PF}_6^-$  at 6 K: (a) view along the  $c$  axis and (b) projection down the  $[1\bar{1}2]$  direction. Both panels display whole molecules in which at least one constituent atom lies within the unit cell; note that the origin of the primitive vectors is shifted for clarity. The orange points represent high-occupancy disordered sites of  $\text{Li}^+$ , while the maroon points represent low-occupancy ones of  $\text{Li}^+$ . The packing structure was visualized using the cif file of Ref. 31 and Mercury 4.0 (C. F. Macrae, I. Sovago, S. J. Cottrell, P. T. A. Galek, P. McCabe, E. Pidcock, M. Platings, G. P. Shields, J. S. Stevens, M. Towler and P. A. Wood, *J. Appl. Cryst.*, 2020, **53**, 226).

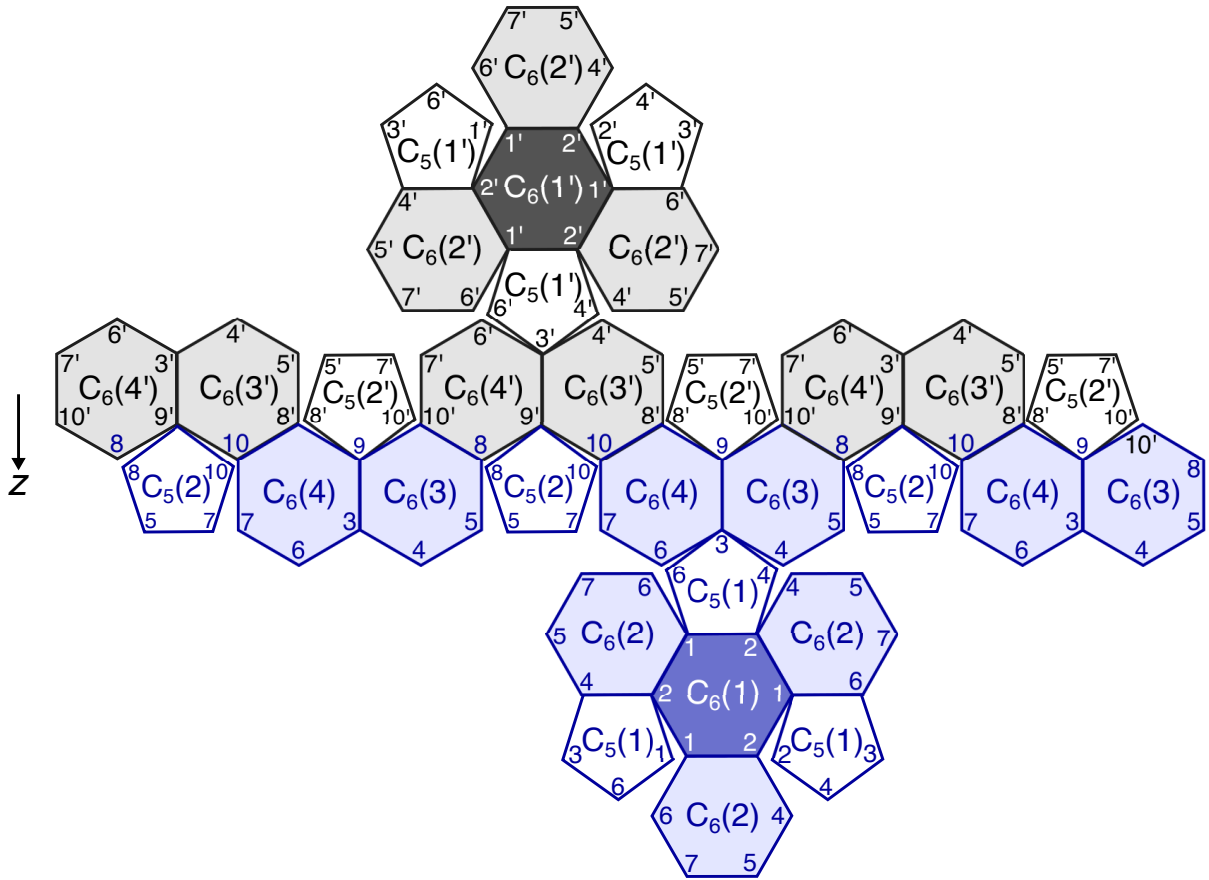


Fig. S2. Unwrapped and flattened map of the  $C_{60}$  cage in the  $[Li^+@C_{60}]6PF_6^-$  (6 K) model. The map shows the symbols for the cage-surface points through which the radial rays (and their equivalent rays) pass. The  $C_{60}$  cage has  $C_3$  symmetry, and any two points denoted by the same symbol are symmetrically equivalent. The rings and carbon sites in the northern hemisphere ( $z > 0$ ) are indicated by blue highlights. The  $C_6(1)$  and  $C_6(1')$  rings and the other  $C_6$  rings are indicated by deep and light colors, respectively. There is a single F atom contacting each of the  $C_6(2)$  and  $C_6(2')$  centers. For a carbon site  $C^j$  ( $j = 1, \dots, 10, 1', \dots, 10'$ ), only the number  $j$  is shown. See Fig. 1 for the original geometry before unwrapping.

Note that in this paper, a chemical bond between two  $C_6$  rings is designated by C=C, and a bond between a  $C_5$  ring and a  $C_6$  ring is designated by C–C, regardless of the actual electronic structure (*e.g.*, bond order indices). Accordingly, a  $C_6$  ring is composed of three C=C bonds and three C–C bonds, whereas a  $C_5$  ring is composed of only C–C bonds.



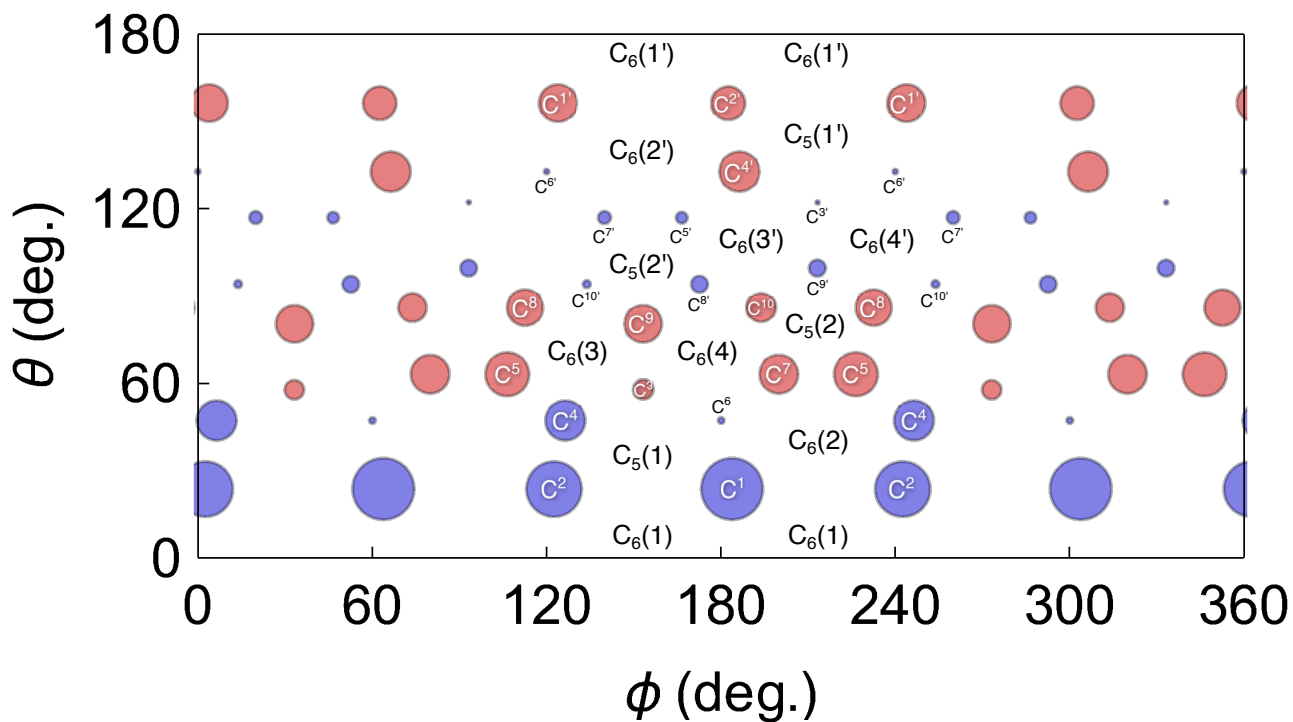


Fig. S4. Radial displacement ( $\Delta r_C$ ) of every C atom in the  $[\text{Li}^+@C_{60}]6\text{PF}_6^-$  (6 K) model relative to the corresponding atom in the  $[\text{Li}^+@C_{60}]6\text{PF}_6^-$  (40 K) model. In the bubble chart, each circle is centered at the  $\theta$  and  $\phi$  angles of a C atom position of the  $[\text{Li}^+@C_{60}]6\text{PF}_6^-$  (6 K) model, and the circle diameter refers to  $|\Delta r_C|$ . The blue circles correspond to the C atoms pulled out from the cage center (*i.e.*,  $\Delta r_C > 0$ ), and the red circles correspond to those pushed toward the center (*i.e.*,  $\Delta r_C < 0$ ). For example, the largest blue circles of the C<sup>1</sup> atoms and the second-largest blue circles of the C<sup>2</sup> atoms indicate positive displacements of 0.0046 and 0.0041 Å, respectively. Given that both geometries have the  $C_3$  axis aligned with the  $z$  axis, not all of the ring and atom positions are indicated by their symbols. The north pole and the south pole are spread out over all azimuth angles  $\phi$  at the bottom ( $\theta = 0^\circ$ ) and the top ( $\theta = 180^\circ$ ) of the chart, respectively.

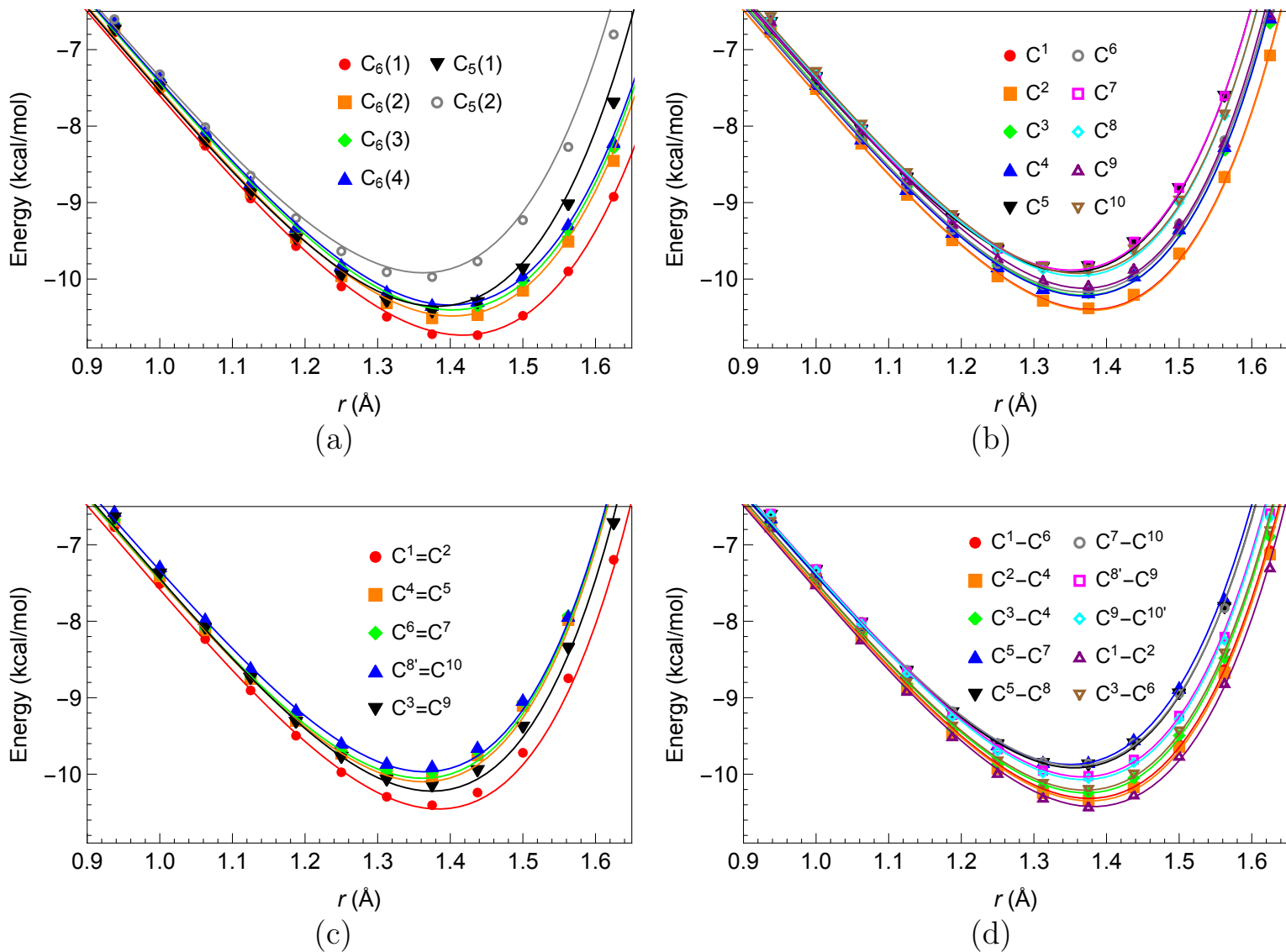


Fig. S5. Radial profiles of the potential energy function  $V_{\text{es+exrep+pol+disp}}^{6\text{K}}$  (curves) along the 31 one-dimensional rays in the northern hemisphere ( $z > 0$ ) of the  $[\text{Li}^+\text{@C}_{60}]\text{6PF}_6^-$  (6 K) model: the rays toward (a) ring centers, (b) C atoms, (c) C=C centers, and (d) C-C centers. The symbols are the single-point RI-MP2 energies,  $\Delta E_{\text{RI-MP2}}$ , which are relative to the energy at  $r = 0 \text{ \AA}$  (*i.e.*, the  $\text{C}_{60}$  cage center). We note that although the energy curve of the  $\text{C}^{8'}=\text{C}^{10}$  ray is shown in panel (c), the  $S_6 \rightarrow C_3$  cage distortion makes the corresponding bond center move from the northern to the southern hemisphere across the equator. See Table S7 for the depths and the radial positions of the minima.

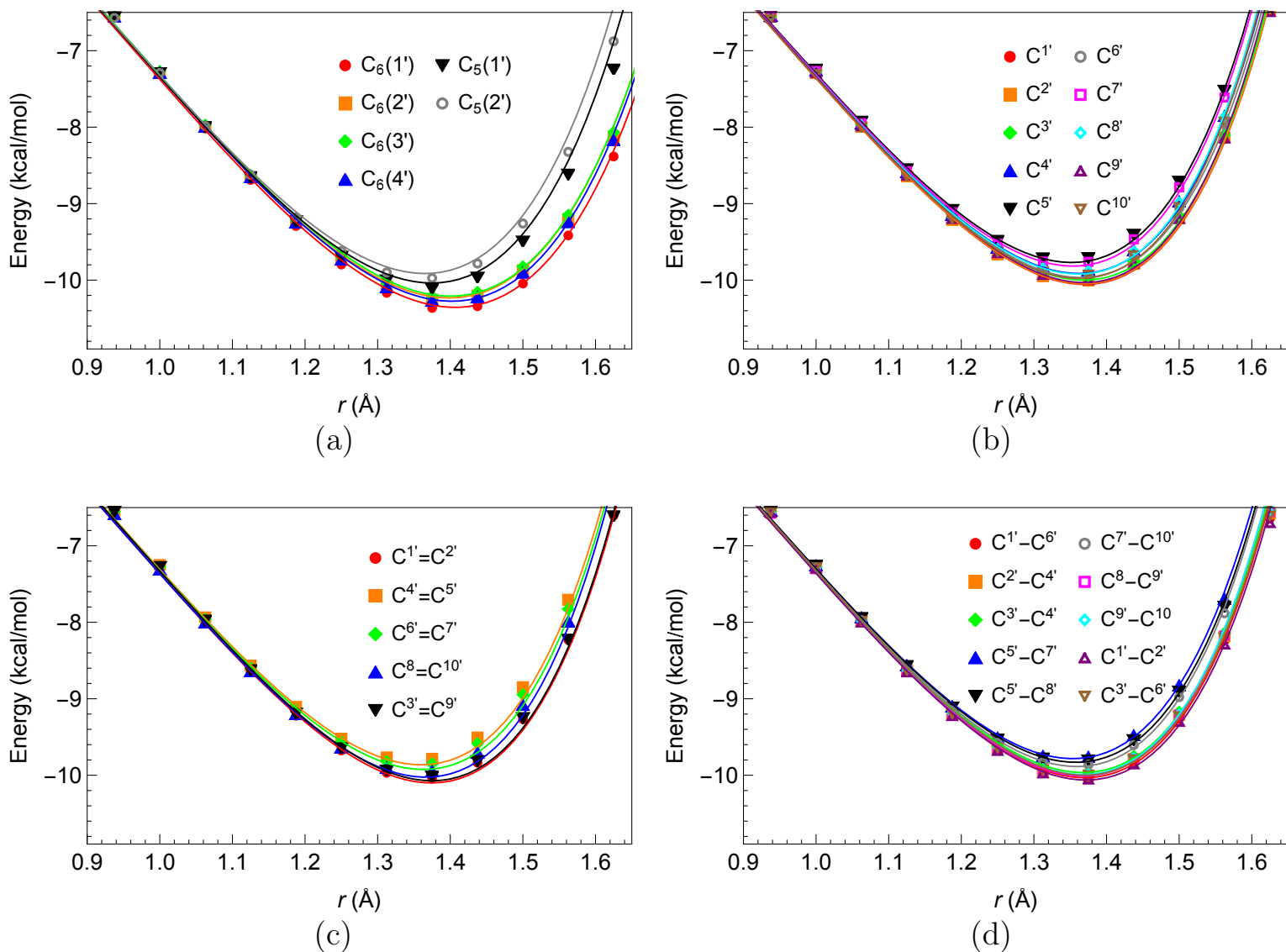
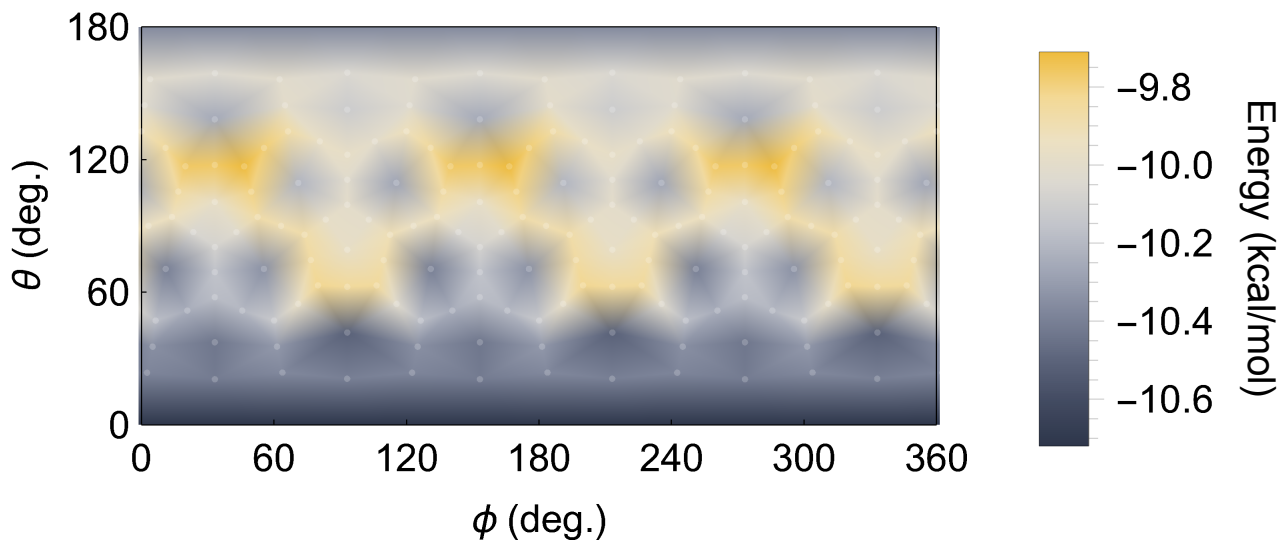
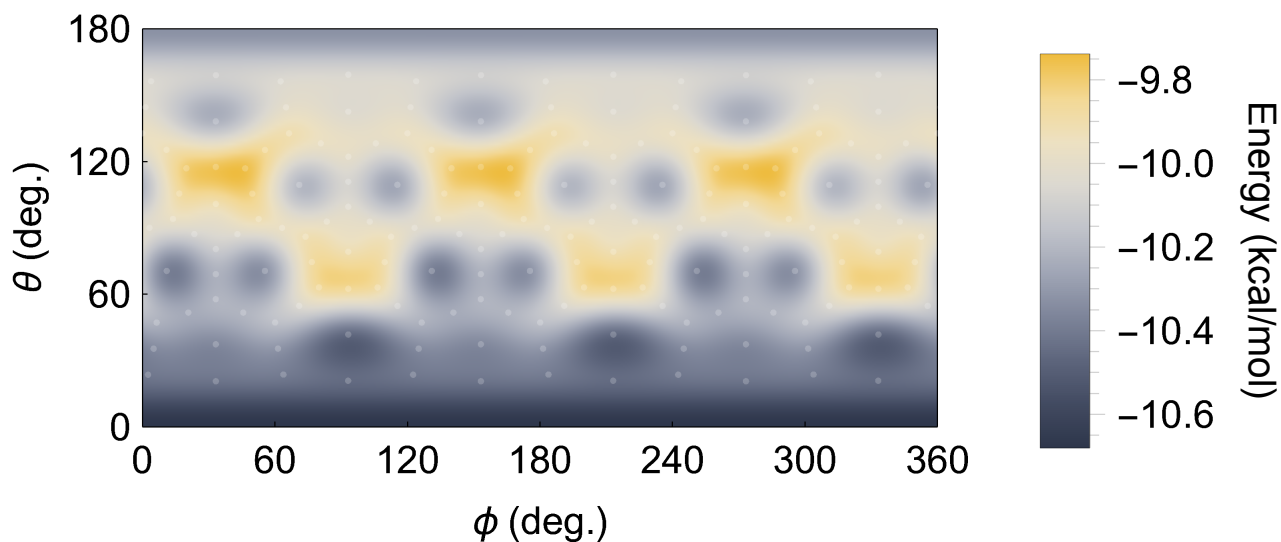


Fig. S6. Radial profiles of the potential energy function  $V_{es+exrep+pol+disp}^{6K}$  (curves) along the 31 one-dimensional rays in the southern hemisphere ( $z < 0$ ) of the  $[\text{Li}^+@C_{60}]6\text{PF}_6^-$  (6 K) model: the rays toward (a) ring centers, (b) C atoms, (c) C=C centers, and (d) C-C centers. The symbols are the single-point RI-MP2 energies,  $\Delta E_{\text{RI-MP2}}$ , which are relative to the energy at  $r = 0 \text{ \AA}$  (*i.e.*, the  $C_{60}$  cage center). See Table S7 for the depths and the radial positions of the minima.



(a) Single-point calculation



(b) Model function

Fig. S7. Polar profiles of the potential energy in a spherical shell with  $r = 1.375 \text{ \AA}$ : (a) the single-point RI-MP2 data,  $\Delta E_{\text{RI-MP2}}$ , and (b) the model function,  $V_{\text{es+exrep+pol+disp}}^{6\text{K}}$ , for the  $[\text{Li}^+@C_{60}]6\text{PF}_6^-$  (6 K) model. The north pole and the south pole are spread out over all azimuth angles  $\phi$  at the bottom ( $\theta = 0^\circ$ ) and the top ( $\theta = 180^\circ$ ) of each map, respectively. The positions underneath the C atoms, bond centers, and ring centers, except those underneath the  $C_6(1)$  and  $C_6(1')$  centers at the two poles, are indicated by semitransparent white points, at which the single-point calculations were performed. The maps were generated by interpolating the data points by means of a Delaunay triangulation. The plot range, shown in each bar legend, was defined using the minimum and maximum energies in the spherical shell.

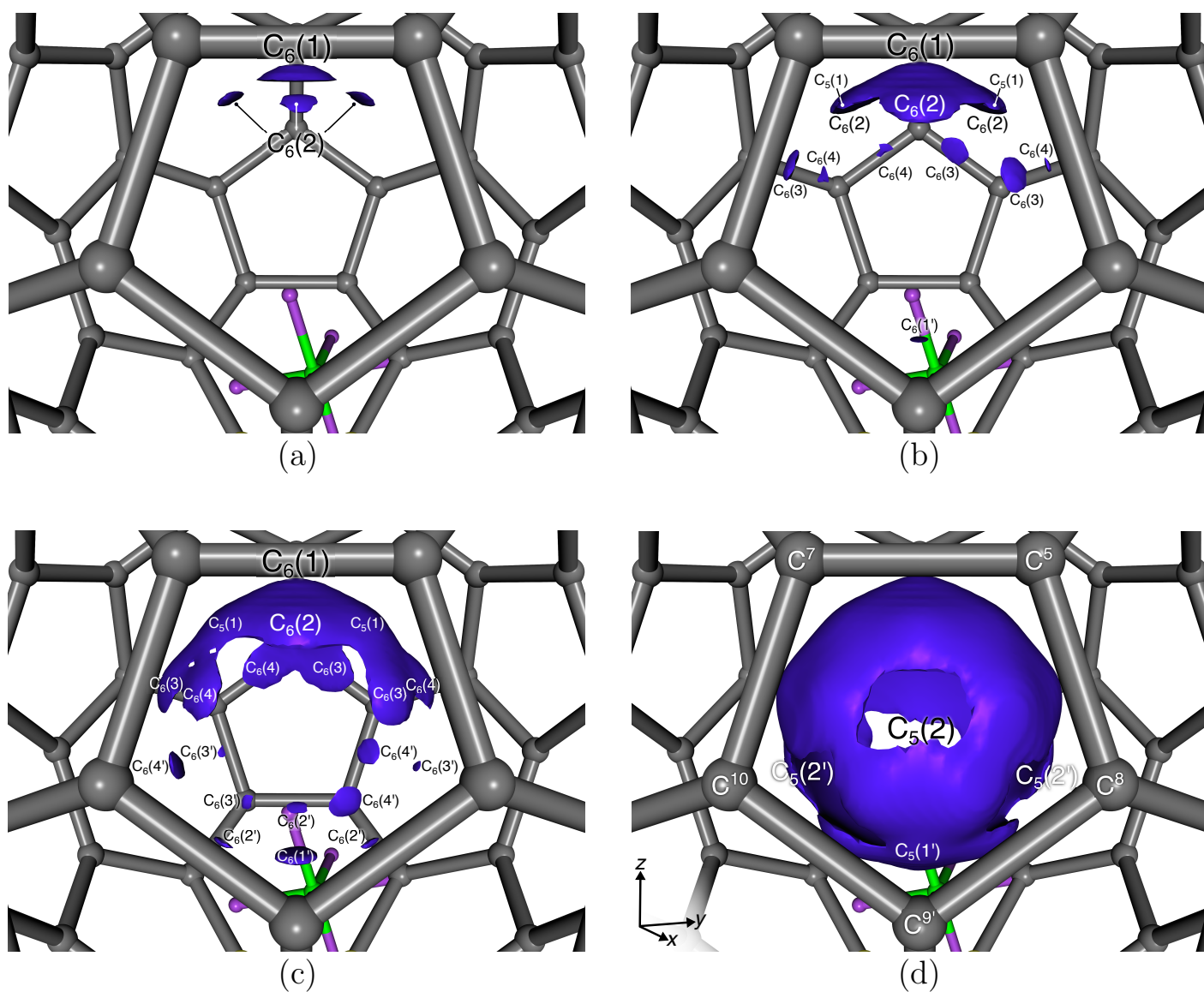
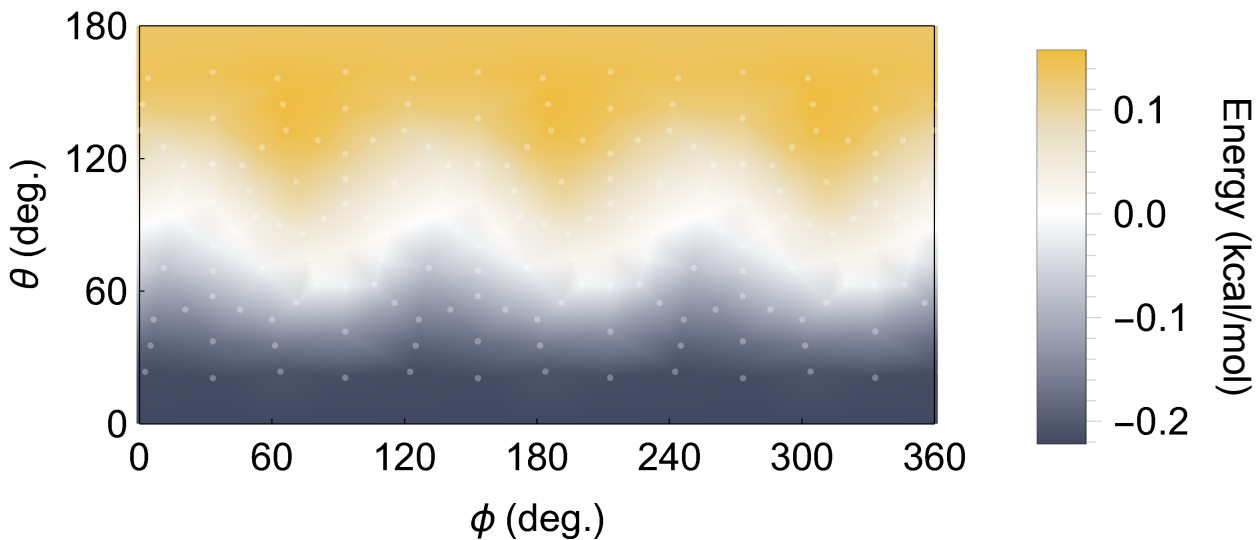


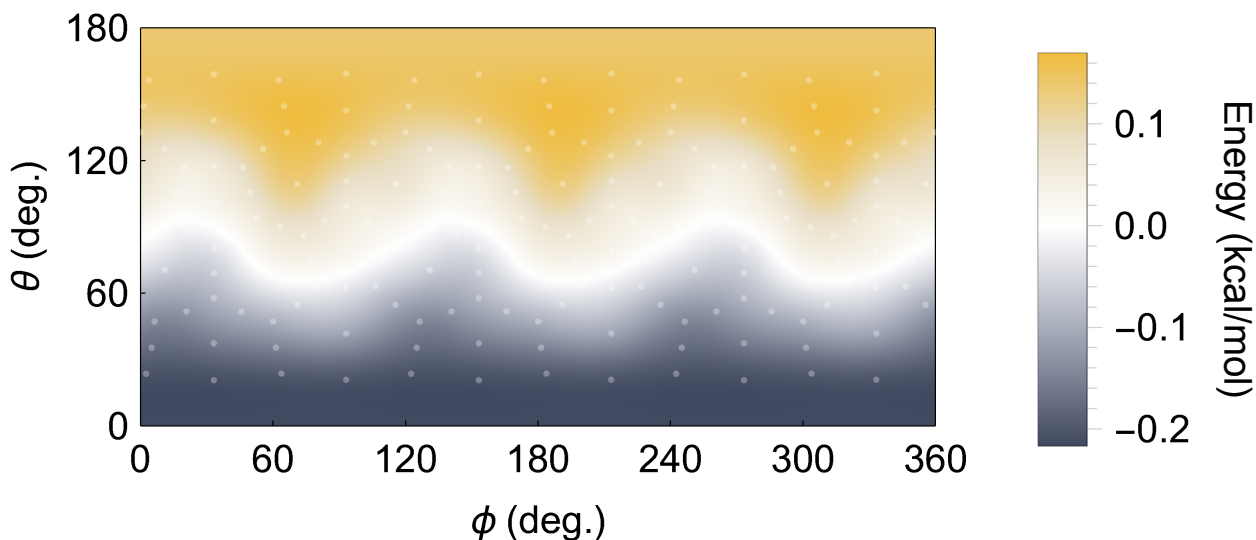
Fig. S8. Isosurfaces of the potential energy function  $V_{es+exrep+pol+disp}^{6K}$  of the  $[Li^+@C_{60}]6PF_6^-$  (6 K) model: side-view plots through a C<sub>5</sub>(2) ring with isovalues of (a) -10.46, (b) -10.32, (c) -10.19, and (d) -9.93 kcal mol<sup>-1</sup>. In panel (d), we show the symbols for the C atoms of the C<sub>5</sub>(2) ring (*i.e.*, C<sup>5</sup>, C<sup>7</sup>, C<sup>8</sup>, C<sup>10</sup>, and C<sup>9'</sup>) and the Cartesian  $xyz$  frame, whose origin is shifted for clarity. See Fig. S2 for the unwrapped geometry of the cage. See the next page for the explanation of this figure.

## Regarding the isosurface plots of the potential energy function $V_{\text{es+exrep+pol+disp}}^{6\text{K}}$ of the $[\text{Li}^+@C_{60}]\text{6PF}_6^-$ (6 K) model

When using an isovalue of  $-10.46 \text{ kcal mol}^{-1}$  (Fig. S8a), we found four islands in the northern hemisphere ( $z > 0$ ) and no islands in the southern hemisphere ( $z < 0$ ). The large isolated island at the north pole corresponds to the deepest  $C_6(1)$  potential well. The three small islands near the  $C_6(1)$  island correspond to the  $C_6(2)$  wells, which are the second deepest among all the ring center wells. When the isovalue is increased to  $-10.32 \text{ kcal mol}^{-1}$  (Fig. S8b), six isolated islands emerge in the northern hemisphere and one at the south pole. The six islands correspond to the  $C_6(3)$  and  $C_6(4)$  wells. The island at the south pole corresponds to the  $C_6(1')$  well. In addition, in the northern hemisphere, there are three tiny islands tied to the large isosurface that encloses the  $C_6(1)$  and  $C_6(2)$  wells. These tiny islands are the shallow  $C_5(1)$  wells. When the isovalue is increased to  $-10.19 \text{ kcal mol}^{-1}$  (Fig. S8c), all of the remaining  $C_6$  wells appear as isolated islands in the southern hemisphere. When the isovalue is increased to  $-9.93 \text{ kcal mol}^{-1}$  (Fig. S8d), a pseudo-spherical hollow appears because all the radial rays exhibit energy minima around  $r = 1.375 \text{ \AA}$  (Fig. S5–S6). The hollow still has six holes, indicating that there are no evident potential wells that restrict the librational motion of  $\text{Li}^+$  underneath the  $C_5(2)$  and  $C_5(2')$  rings. The hollow is continuous underneath the  $C_5(1')$  rings due to the shallow  $C_5(1')$  wells.

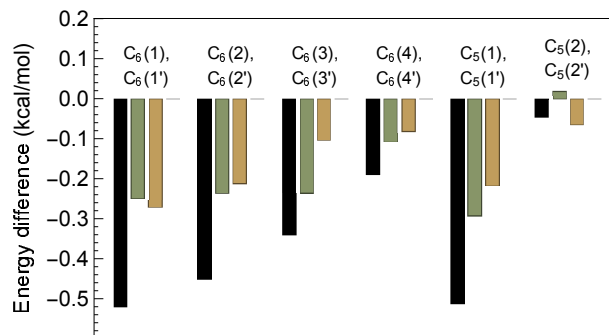


(a) Single-point calculation

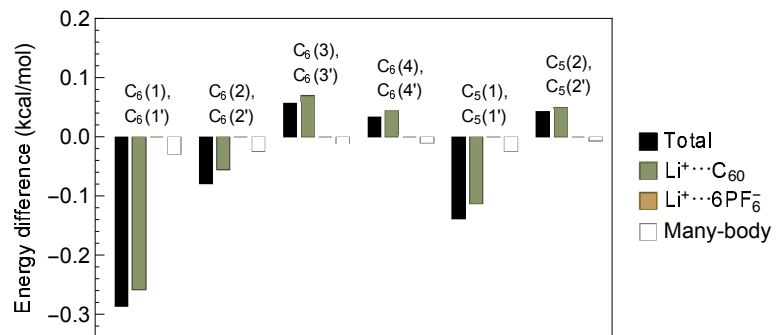


(b) Model function

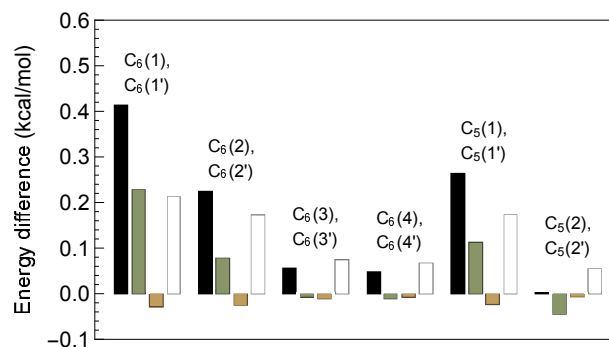
Fig. S9. Polar plot of the differential potential energy profile associated with the  $S_6 \rightarrow C_3$  cage distortion: (a) the change in the  $\Delta E_{\text{RI-MP2}}$  grid data and (b) the change in the model function for the  $[\text{Li}^+@C_{60}]6\text{PF}_6^-$  (6 K) model relative to the data for the  $[\text{Li}^+@C_{60}]6\text{PF}_6^-$  (40 K) model (*i.e.*,  $V_{\text{es+exrep+pol+disp}}^{6\text{K}} - V_{\text{es+exrep+pol+disp}}^{40\text{K}}$  in panel (b) and the corresponding single-point calculation data in panel (a)). Both image maps are polar plots in a spherical shell with  $r = 1.375 \text{ \AA}$ . The positions underneath the C atoms, bond centers, and ring centers of the  $[\text{Li}^+@C_{60}]6\text{PF}_6^-$  (6 K) model, except those underneath the  $C_6(1)$  and  $C_6(1')$  centers at the two poles, are indicated by semitransparent white points. Although the distortion makes the  $\theta$  and  $\phi$  angles of the grid data of the  $[\text{Li}^+@C_{60}]6\text{PF}_6^-$  (6 K) model slightly different from those of the  $[\text{Li}^+@C_{60}]6\text{PF}_6^-$  (40 K) model, such differences were ignored in the energy subtraction to obtain panel (a). The maps were generated by interpolating the data points by means of a Delaunay triangulation. The plot range, shown in each bar legend, was defined using the minimum and maximum values in the spherical shell.



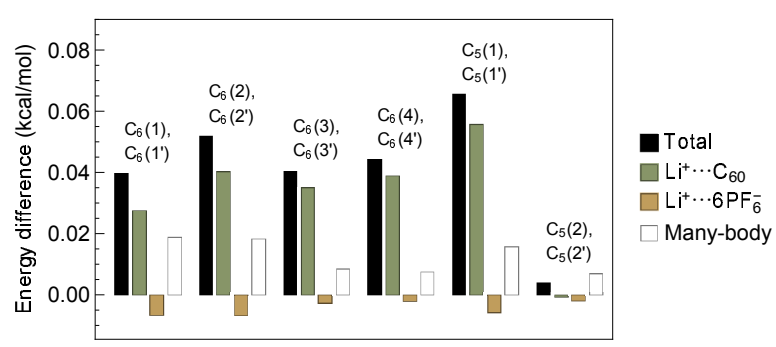
(a) es



(b) exrep

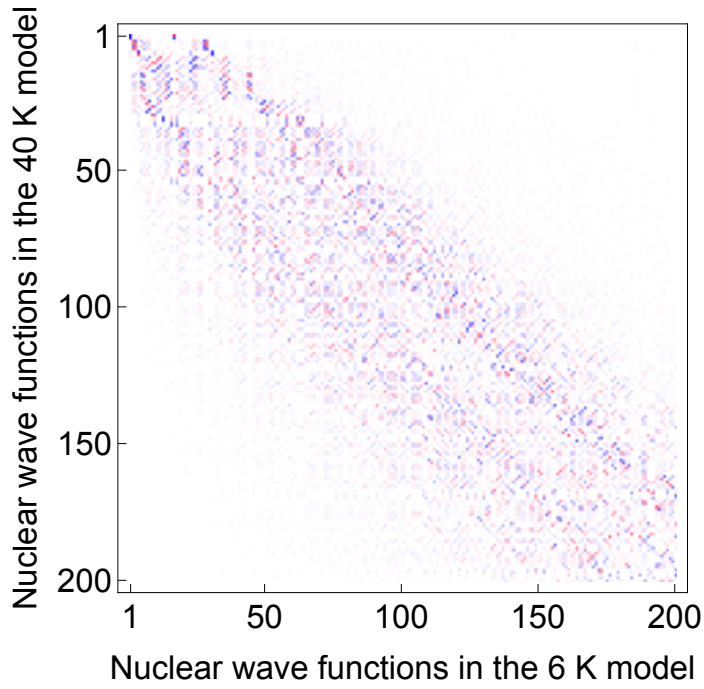


(c) pol

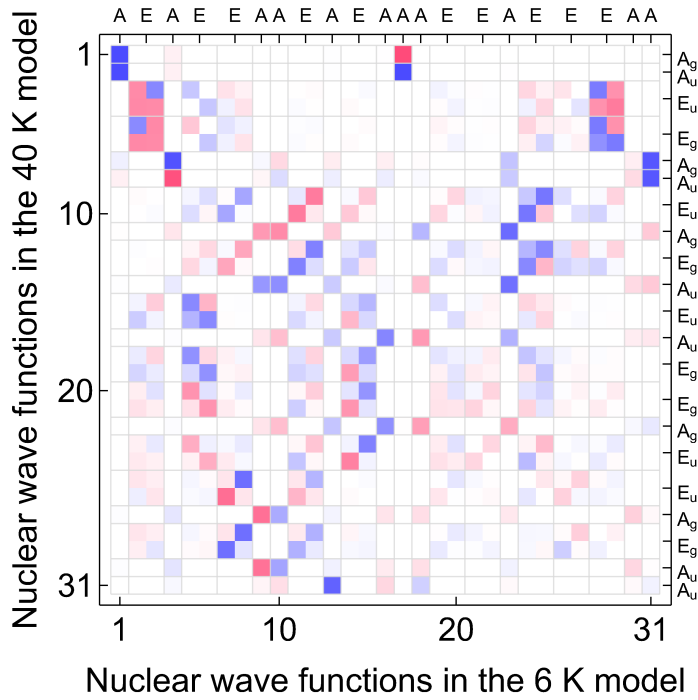


(d) disp

Fig. S10. Fragment pair decomposition of the four EDA components in Fig. 4, each of which is defined by  $E_\alpha(x, y, z) - E_\alpha(x', y', z') = \Delta E_\alpha(x, y, z) - \Delta E_\alpha(x', y', z')$  ( $\alpha = \text{es, exrep, pol, or disp}$ ). Here,  $(x, y, z)$  and  $(x', y', z')$  are the approximate positions ( $r = 1.375 \text{ \AA}$ ) of a northern well and its southern counterpart, respectively. The results of the fragment pair decomposition of  $\Delta E_\alpha(x, y, z)$  and  $\Delta E_\alpha(x', y', z')$  are listed in Tables S8 and S9, respectively, and simple subtractions of the results in Table S9 from those in Table S8 yield the bar charts presented here.

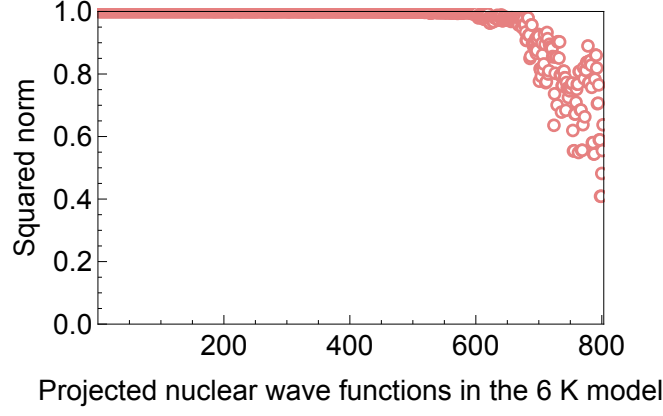


(a)

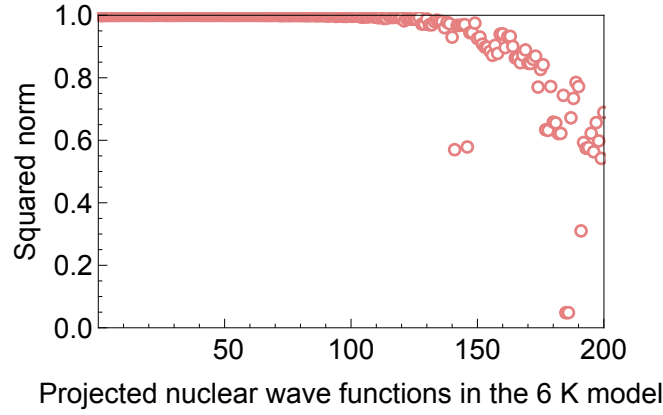


(b)

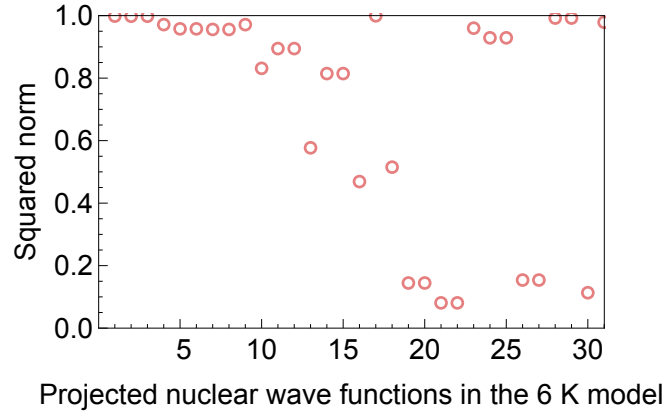
Fig. S11. Overlap matrix  $S$  for the set of nuclear states of  $\text{Li}^+$  in the  $[\text{Li}^+@C_{60}]6\text{PF}_6^-$  (40 K) model,  $|\psi_k^{40\text{K}}\rangle$  ( $k = 1, 2, \dots, 801$ ), and that in the  $[\text{Li}^+@C_{60}]6\text{PF}_6^-$  (6 K) model,  $|\psi_l^{6\text{K}}\rangle$  ( $l = 1, 2, \dots, 802$ ). Both sets of the nuclear states are arranged in the order of increasing energy. The positive and negative overlap elements of (a) the  $200 \times 200$  submatrix and (b) the  $31 \times 31$  submatrix (*i.e.*, low-energy blocks of  $S$ ) are represented by blue and pink colors, respectively. Deeper color indicates a larger absolute value. In panel (b), a gray mesh is used to visually partition the matrix into every irreducible-representation block. See Fig. S12 for the squared norm of every column of  $S$  and its submatrices.



(a)

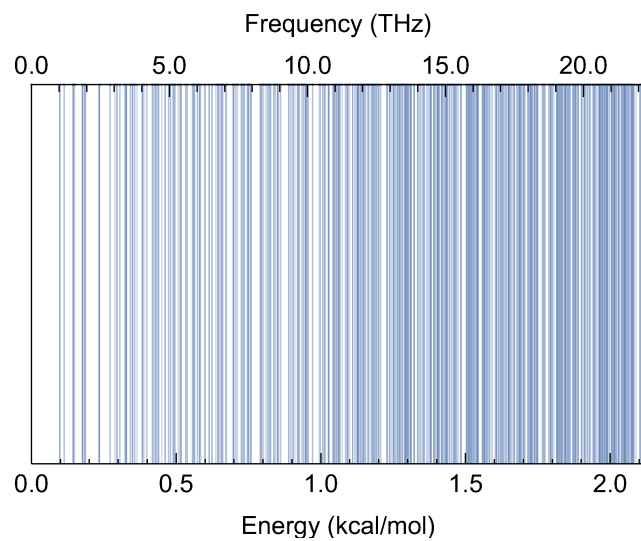


(b)

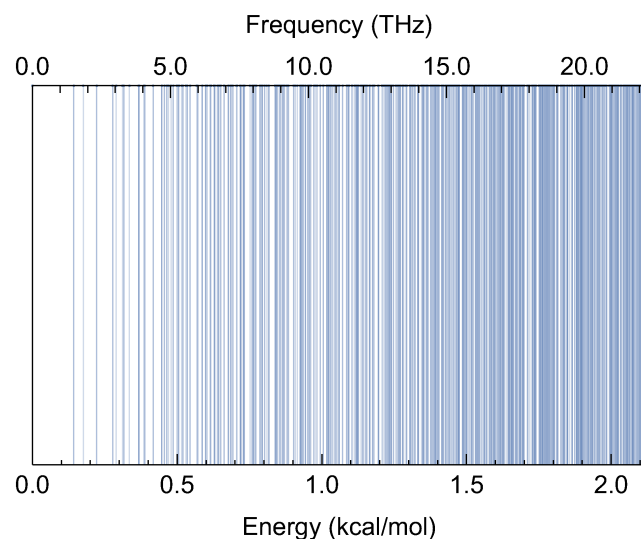


(c)

Fig. S12. Squared norm of each column of overlap matrix  $S$  and its submatrices. The squared norms are expressed as  $\|\hat{P}|\psi_l^{6\text{K}}\rangle\|^2$  ( $l = 1, 2, \dots, N_l$ ), where  $\hat{P}$  is the projection operator onto the subspace  $P$  spanned by  $|\psi_k^{40\text{K}}\rangle$  ( $k = 1, 2, \dots, N_k$ ). Panels (a), (b) and (c) show the results for  $(N_k, N_l) = (801, 802)$ ,  $(200, 200)$ , and  $(31, 31)$ , respectively. If the squared norm of a projected vector,  $\hat{P}|\psi_l^{6\text{K}}\rangle$ , is 1, it indicates that the inversion-symmetry breaking causes a superposition within the low-energy subspace  $P$  to form  $|\psi_l^{6\text{K}}\rangle$ .



(a) 40 K model



(b) 6 K model

Fig. S13. Nuclear energy levels of  $\text{Li}^+$  in (a) the  $[\text{Li}^+@C_{60}]\text{6PF}_6^-$  (40 K) model and (b) the  $[\text{Li}^+@C_{60}]\text{6PF}_6^-$  (6 K) model. In each panel, the energies are relative to the ground-state energy.

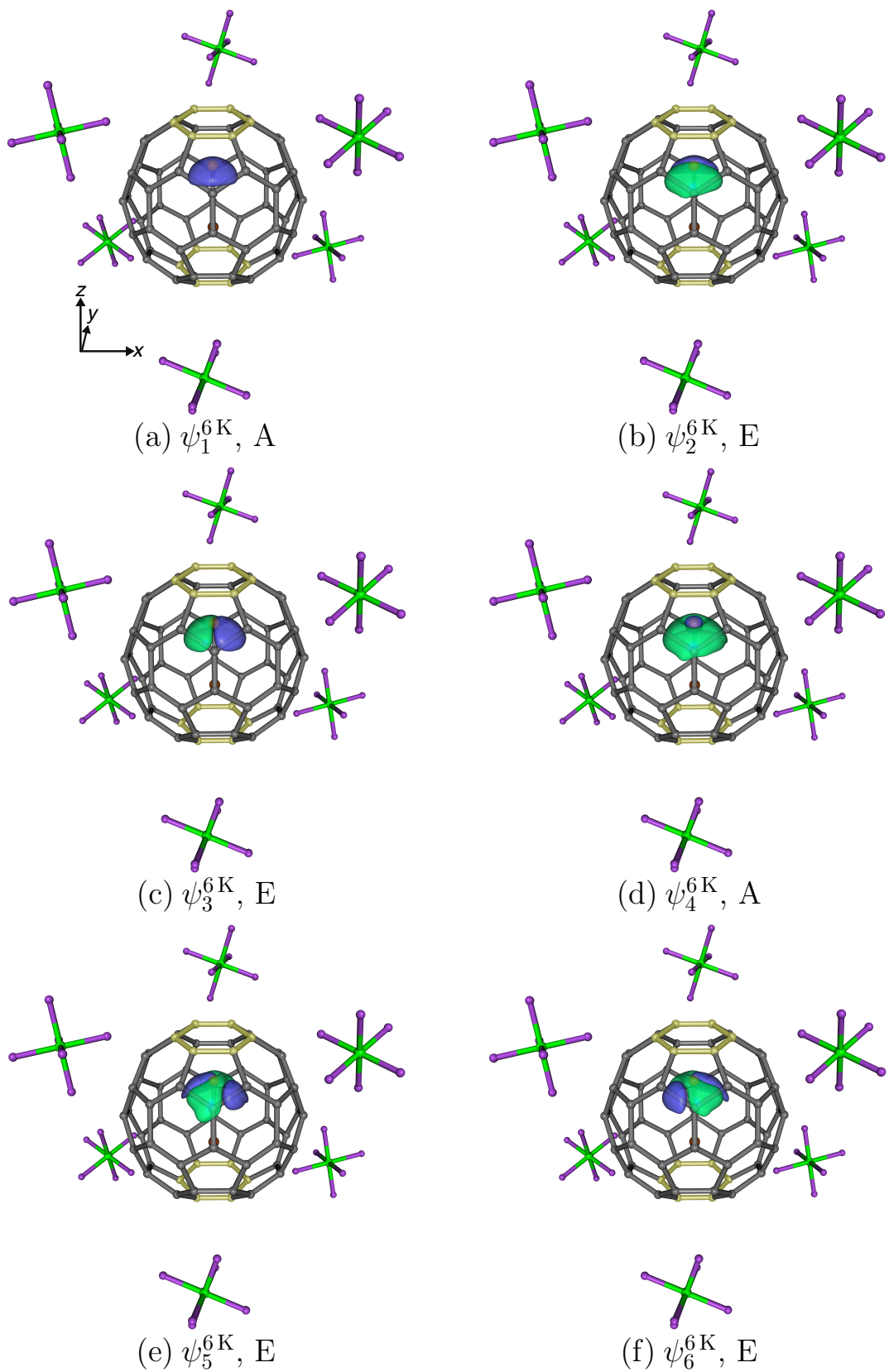


Fig. S14. Isosurface plots (side view) of nuclear wave functions of  $\text{Li}^+$  in the  $[\text{Li}^+@C_{60}]6\text{PF}_6^-$  (6 K) model, which are selected from low-energy ones and presented in the order of increasing energy. The symbol and the irreducible representation (*i.e.*, A or E) of every wave function are given in the subfigure captions. The blue and green isosurfaces were generated using the isovalues of  $\pm 0.02 \text{ bohr}^{-3/2}$ . Underneath the  $C_6(1)$  ring and the  $C_6(1')$  ring, indicated by yellow highlights, there are the high-occupancy disordered site (*i.e.*, the orange point) and the low-occupancy one (*i.e.*, the maroon point), respectively.

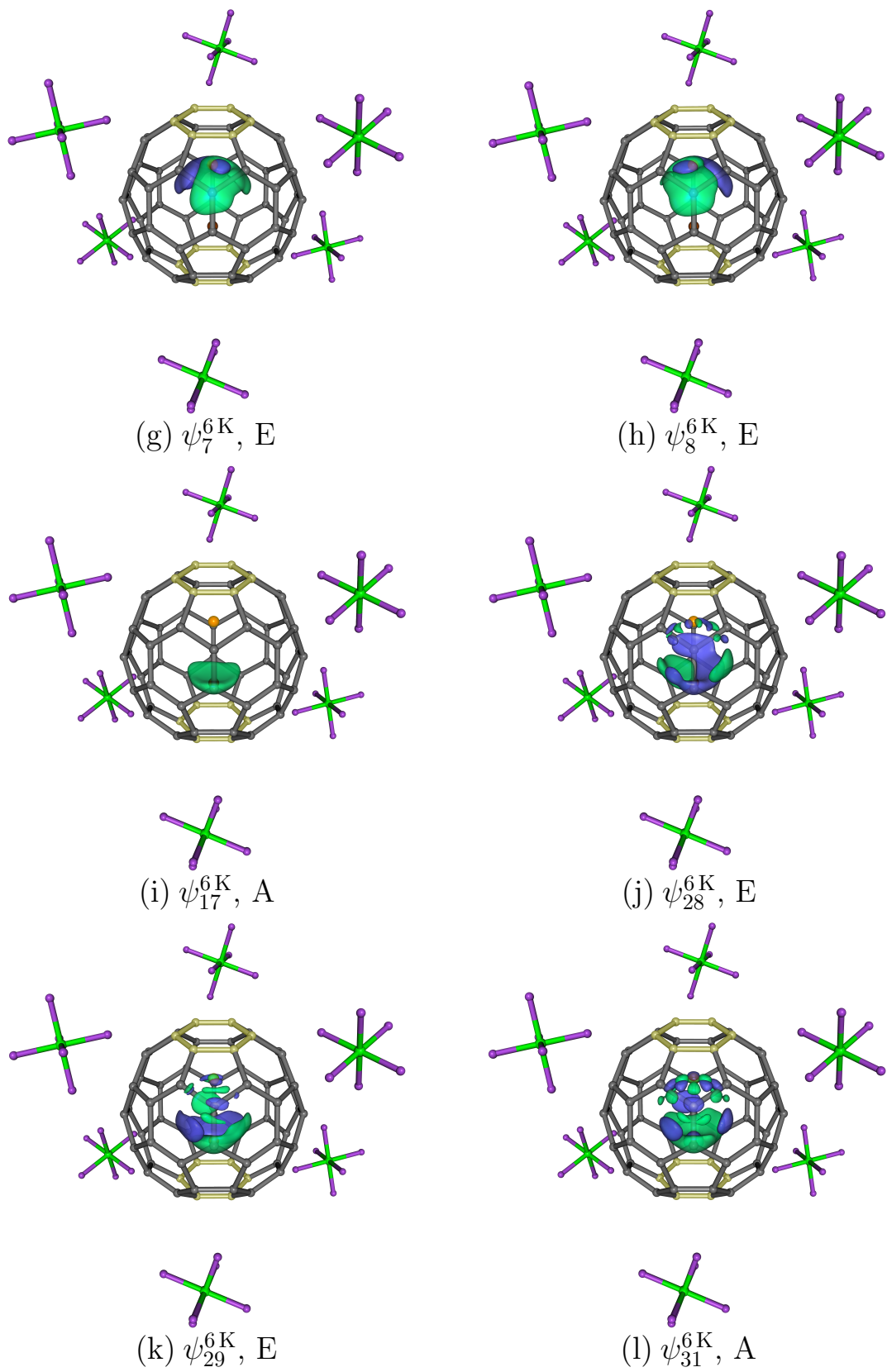


Fig. S14. (Continued)

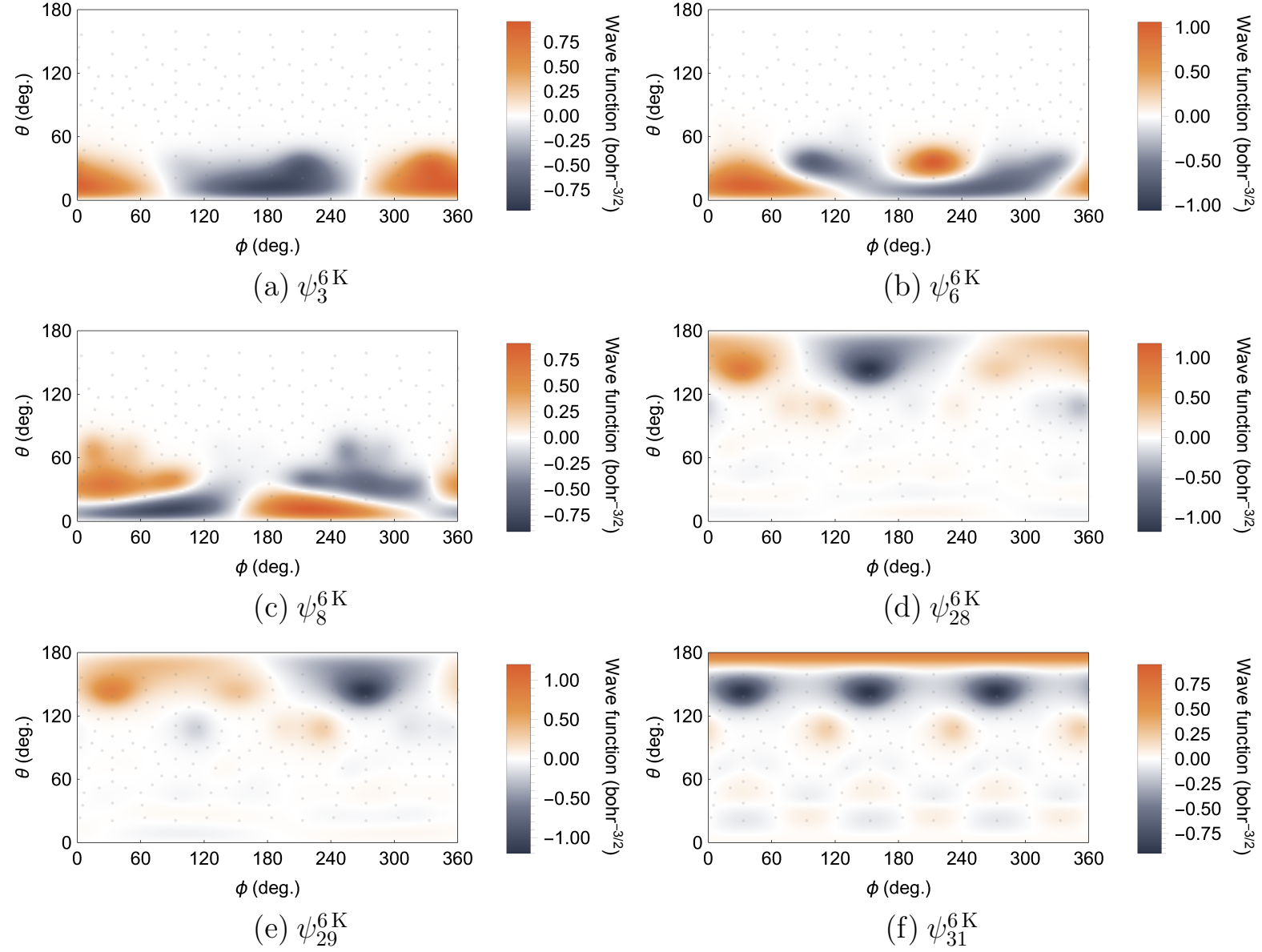
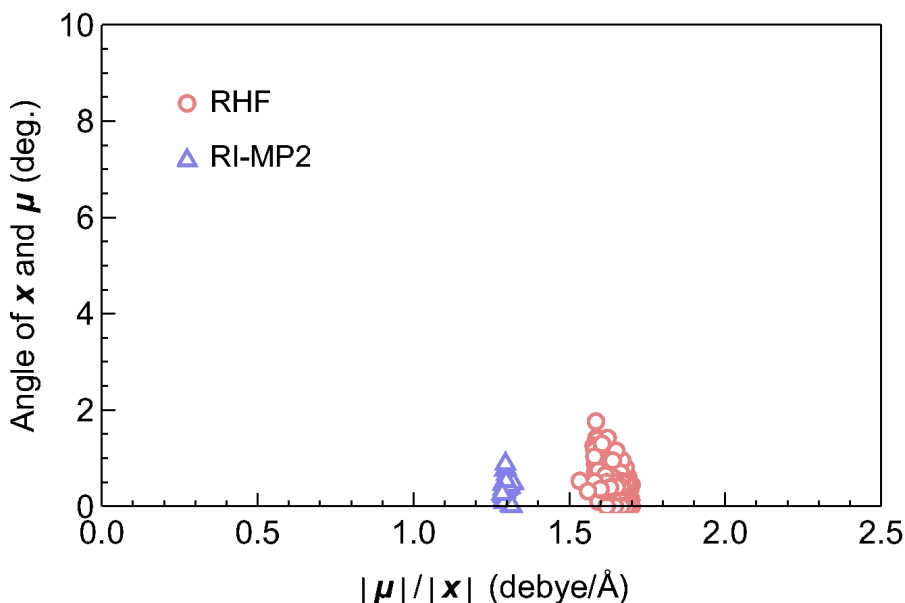
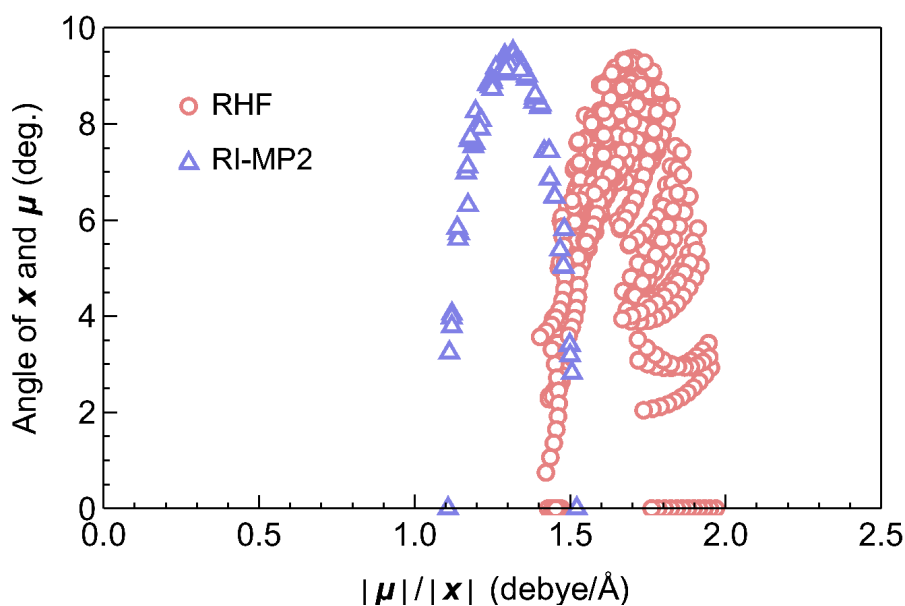


Fig. S15. Polar plots of excited-state nuclear wave functions of  $\text{Li}^+$  in the  $[\text{Li}^+\text{@C}_{60}]\text{6PF}_6^-$  (6 K) model, which are presented in the order of increasing energy. The radial distance  $r$  is 1.375 Å. Every wave function belongs to the irreducible representation E, except for (f)  $\psi_{31}^{6K}$  with the irreducible representation A. Each of (a)  $\psi_3^{6K}$ , (b)  $\psi_6^{6K}$ , and (c)  $\psi_8^{6K}$  forms a basis for the degenerate representation E, together with  $\psi_2^{6K}$ ,  $\psi_5^{6K}$ , and  $\psi_7^{6K}$  (Table 2 and Fig. 6), respectively. They have large amplitudes in the northern hemisphere, whereas (d)  $\psi_{28}^{6K}$  and (e)  $\psi_{29}^{6K}$ , which form a basis for the degenerate representation E, and (f)  $\psi_{31}^{6K}$  have large amplitudes in the southern hemisphere. The positions underneath the C atoms, bond centers, and ring centers, except those underneath the  $\text{C}_6(1)$  and  $\text{C}_6(1')$  centers, are indicated by gray points. The plot range, shown in each bar legend, was determined using the largest amplitude on the shell with  $r = 1.375$  Å.



(a)



(b)

Fig. S16. Numerical evaluation of the dipole-moment approximation,  $\boldsymbol{\mu} \propto \boldsymbol{x}$ , in (a) the  $[\text{Li}^+@C_{60}]6\text{PF}_6^-$  (40 K) model and (b) the  $[\text{Li}^+@C_{60}]6\text{PF}_6^-$  (6 K) model. The two scatter plots show the distributions of the angle of  $\boldsymbol{x}$  and  $\boldsymbol{\mu}$  and the quotient  $|\boldsymbol{\mu}|/|\boldsymbol{x}|$  for low-energy geometries, where  $\boldsymbol{x}$  is the position vector of  $\text{Li}^+$ ,  $(x, y, z)$ , and  $\boldsymbol{\mu}$  is the electronic expectation value of the dipole moment of the whole model. The red circles were obtained using the dipole moments of restricted Hartree–Fock (RHF) calculations. In any of the single-point RHF calculations,  $\text{Li}^+$  was placed at a low-energy grid point, where  $\Delta E_{\text{RI-MP2}} \leq -7.0 \text{ kcal mol}^{-1}$ , and the  $C_{60}$  cage center was chosen as the coordinate origin. The blue triangles were obtained using the dipole moments that we calculated with the RI-MP2 method and the finite field scheme. In these RI-MP2 calculations,  $\text{Li}^+$  was placed at  $r = 1.375 \text{ \AA}$  on every radial ray, near the potential energy minimum along a ray.

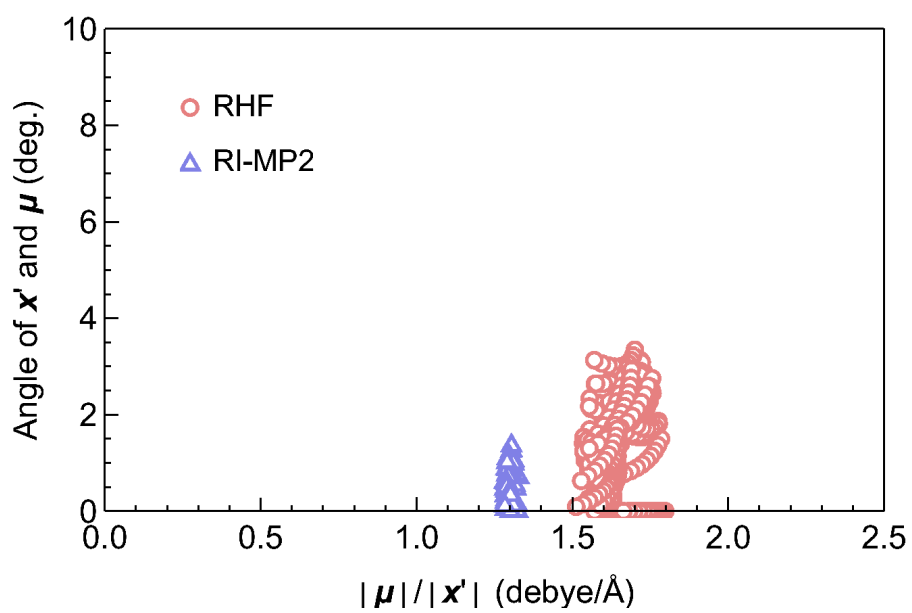


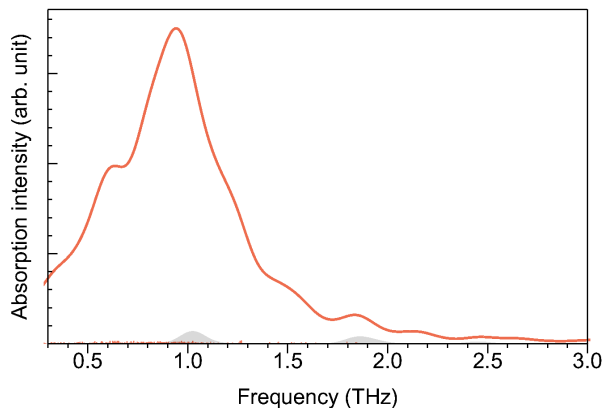
Fig. S17. A refined approximation of the dipole moment of the  $[\text{Li}^+@C_{60}]6\text{PF}_6^-$  (6 K) model,  $\boldsymbol{\mu} \propto \mathbf{x}' := (x, y, z + 0.205 \text{ \AA})$ . The scatter plot shows the distribution of the angle of  $\mathbf{x}'$  and  $\boldsymbol{\mu}$  and the quotient  $|\boldsymbol{\mu}|/|\mathbf{x}'|$  for the low-energy geometries examined in Fig. S16b. See the next page for the detailed explanation of this figure and Fig. S16.

## Numerical evaluation of the approximation of the dipole moment

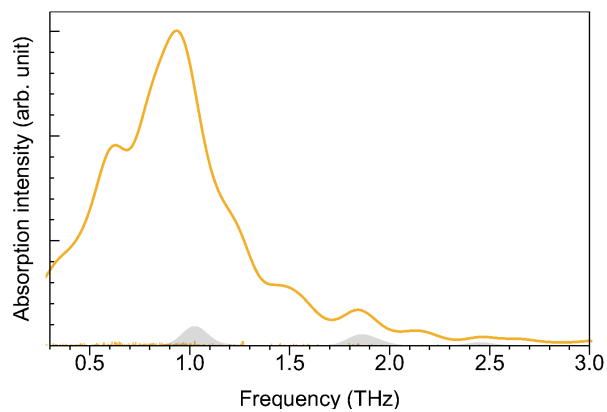
In the  $[\text{Li}^+\text{@C}_{60}]\text{6PF}_6^-$  (40 K) model, the  $\text{C}_{60} \cdot \text{6PF}_6^-$  framework is inversion-symmetric. With the  $\text{C}_{60}$  cage center placed at the coordinate origin, the framework has no dipole moment. The norm of the dipole moment of the entire model,  $|\boldsymbol{\mu}|$ , is zero if  $\text{Li}^+$  is at the origin, while it increases upon the off-centering of  $\text{Li}^+$ . The dipole-moment approximation used in Section III E,  $\boldsymbol{\mu} \propto \boldsymbol{x} := (x, y, z)$ , is accurate for the  $[\text{Li}^+\text{@C}_{60}]\text{6PF}_6^-$  (40 K) model; in fact, the angle of  $\boldsymbol{x}$  and  $\boldsymbol{\mu}$  is small and the quotient  $|\boldsymbol{\mu}|/|\boldsymbol{x}| \approx \text{const.}$  for most of the low-potential-energy geometries (Fig. S16a).

In the  $[\text{Li}^+\text{@C}_{60}]\text{6PF}_6^-$  (6 K) model, the dipole moment of the  $\text{C}_{60} \cdot \text{6PF}_6^-$  framework, calculated with respect to the  $\text{C}_{60}$  cage center (origin), is small but not negligible. The dipole moment points in the positive direction of the  $z$  axis (Fig. 1), and the relevant  $z$  component, obtained using the RI-MP2 method and the finite field scheme, is +0.27 debye. Consequently,  $\boldsymbol{\mu}$  is nearly zero when  $\text{Li}^+$  is placed at  $-0.205 \text{ \AA}$  on the  $z$  axis, not at the origin. Meanwhile, the dipole-moment approximation,  $\boldsymbol{\mu} \propto \boldsymbol{x}$ , assumes that  $\boldsymbol{\mu} = \mathbf{0}$  when  $\text{Li}^+$  is at the origin. The discrepancy worsens the accuracy of the approximation somewhat (Fig. S16b). A refined approximation is achieved simply by shifting  $\boldsymbol{x}$  by a constant vector, namely  $\boldsymbol{\mu} \propto (x, y, z + 0.205 \text{ \AA}) =: \boldsymbol{x}'$ . The refined approximation (Fig. S17) is almost as accurate as the approximation for the  $[\text{Li}^+\text{@C}_{60}]\text{6PF}_6^-$  (40 K) model (Fig. S16a).

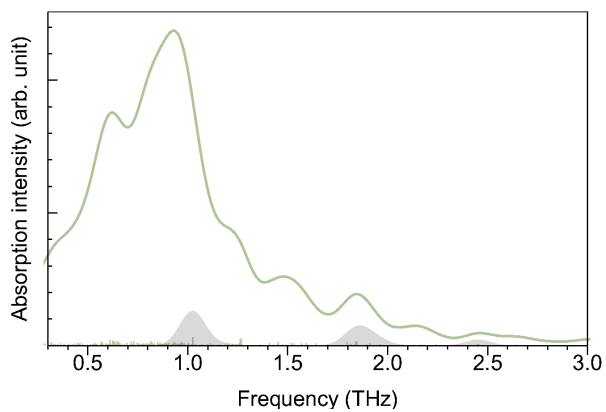
More importantly, however, the use of  $\boldsymbol{x}'$ , instead of  $\boldsymbol{x}$ , as a surrogate for  $\boldsymbol{\mu}$  in eqn (16) does not change the THz absorption spectra of the  $[\text{Li}^+\text{@C}_{60}]\text{6PF}_6^-$  (6 K) model at all. One obtains exactly the same spectra as long as the assumption of the linear relationship between  $\boldsymbol{\mu}$  and the  $\text{Li}^+$  position,  $\boldsymbol{\mu} \propto \boldsymbol{x} + \boldsymbol{C}$ , holds. Here,  $\boldsymbol{C}$  is an arbitrary constant vector, and any integrals including it vanish because of the orthogonality of different nuclear wave functions. In summary, a central assumption of our THz spectrum calculations is the linear relationship between  $\boldsymbol{\mu}$  and  $\boldsymbol{x}$ , not the specific choice of  $\boldsymbol{C}$ . The assumption was numerically justified by the distributions in Fig. S16a and S17.



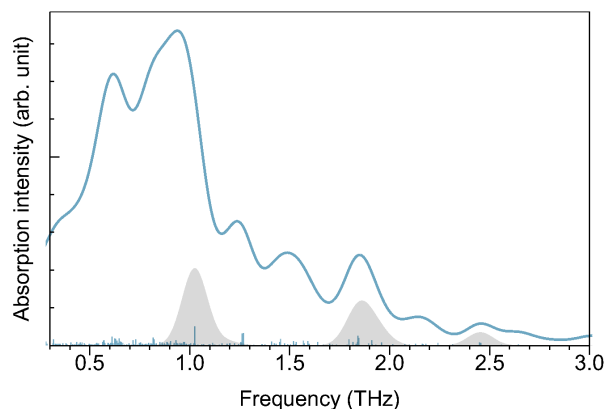
(a) 120 K



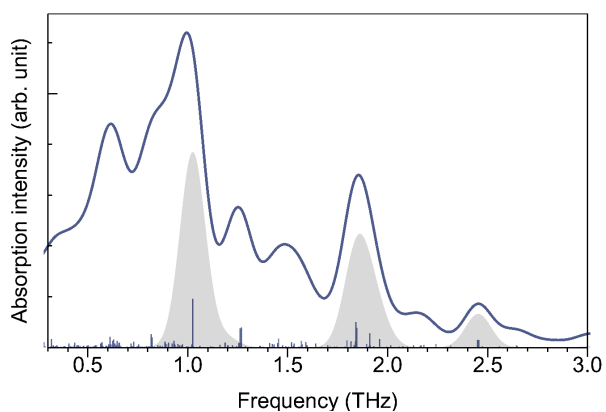
(b) 100 K



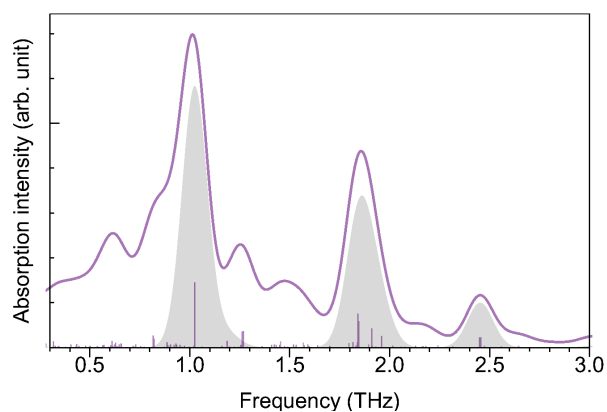
(c) 80 K



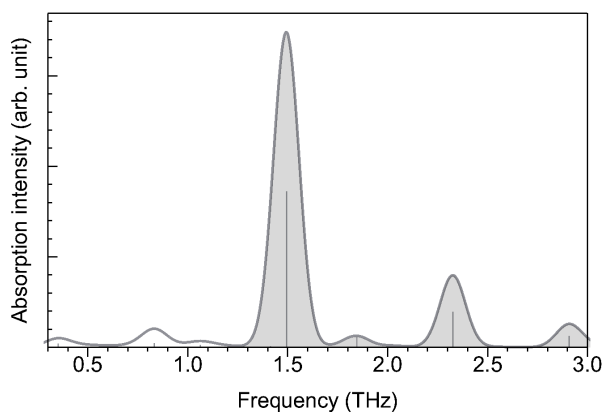
(d) 60 K



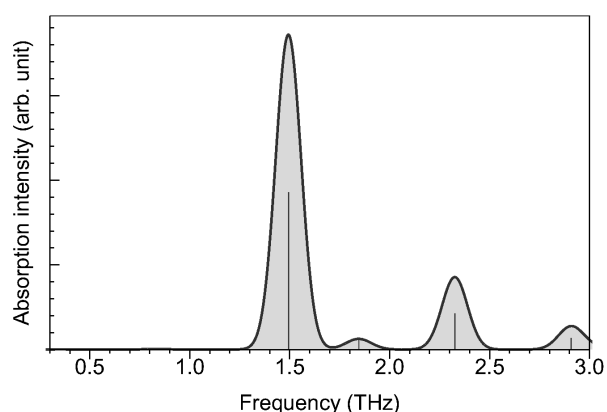
(e) 40 K



(f) 30 K

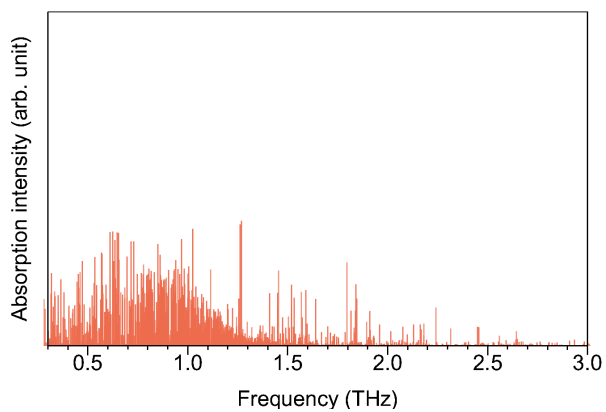


(g) 20 K

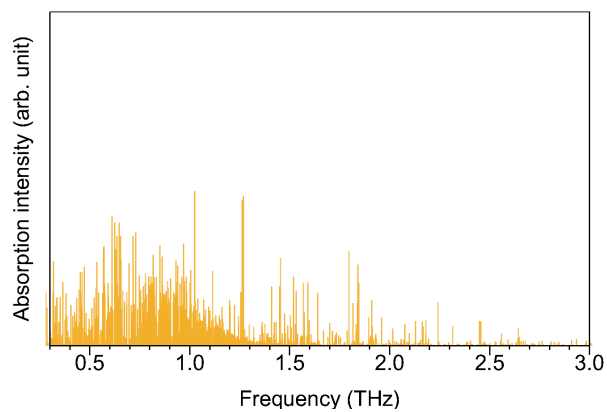


(h) 10 K

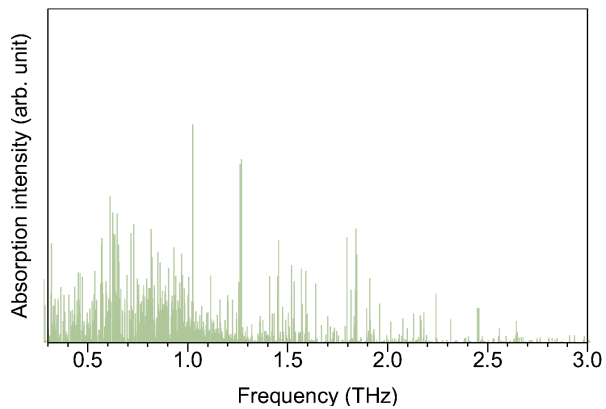
Fig. S18. Theoretical stick spectra of the  $[\text{Li}^+\text{C}_{60}]\text{PF}_6^-$  salt and the spectra convoluted with a Gaussian function with an FWHM of  $5 \text{ cm}^{-1}$  ( $\approx 0.15 \text{ THz}$ ). The shaded spectra represent the contributions of the transitions from the ground state. The plotting range of the absorption intensities was determined to include the whole spectral profile in each panel. The major and minor tick intervals are the same in all the panels.



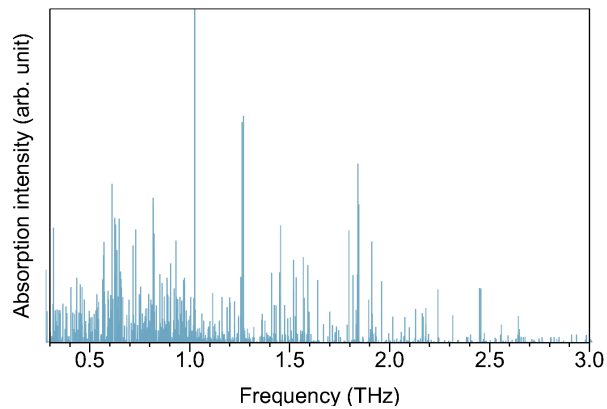
(a) 120 K



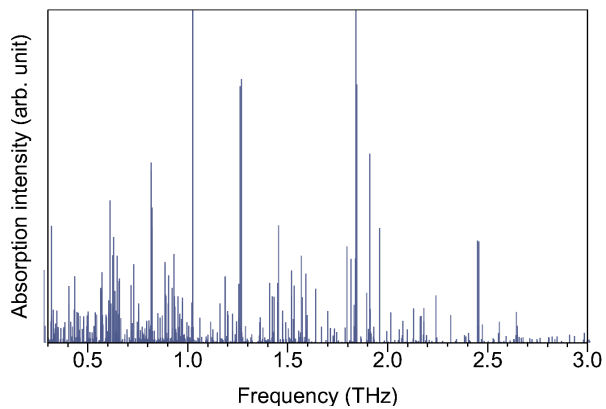
(b) 100 K



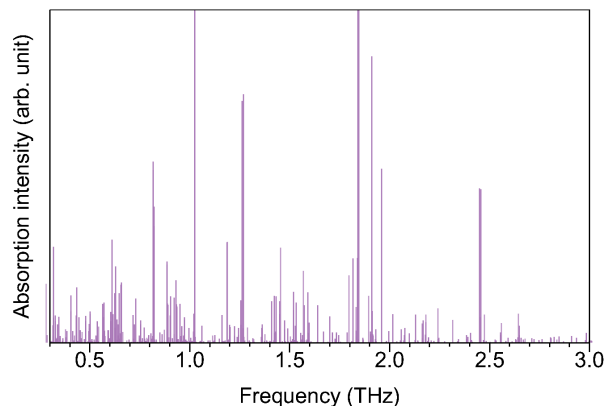
(c) 80 K



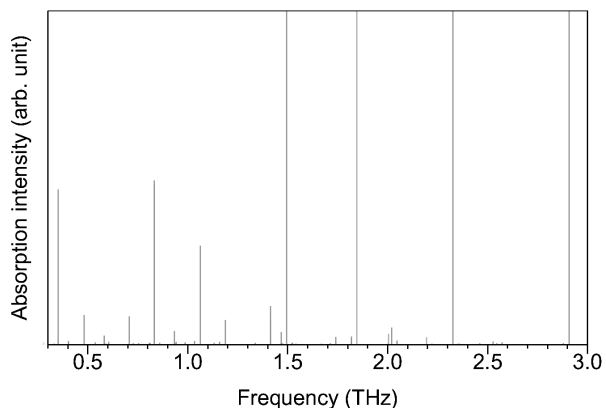
(d) 60 K



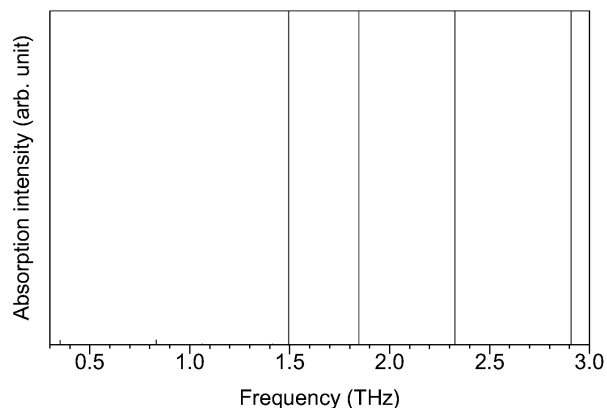
(e) 40 K



(f) 30 K



(g) 20 K



(h) 10 K

Fig. S19. Theoretical stick spectra of the  $[\text{Li}^+\text{@C}_{60}]\text{PF}_6^-$  salt. This figure zooms in on the low-intensity region below half of the first minor tick of Fig. S18.